Discrete-time Design and Stability Analysis for Nonlinear Incremental Fault-tolerant Flight Control

Chang, J.; De Breuker, R.; Wang, Xuerui

Important note
To cite this publication, please use the final published version (if applicable).
Please check the document version above.

Discrete-time Design and Stability Analysis for Nonlinear Incremental Fault-Tolerant Flight Control

Jing Chang* , Roeland De Breuker† and Xuerui Wang‡

Shool of Aerospace Science and Technology, Xidian University, Xi'an, 710072, China
Delft University of Technology, Delft, Zuid-Holland, 2629HS, The Netherlands

Incremental control, including incremental nonlinear dynamic inversion (INDI) and incremental backstepping (IBS), is a sensor-based control framework that enhances the control robustness by exploiting sensor measurements. Although its effectiveness has been demonstrated on various aerospace systems, the explicit and quantifiable expression for the ultimate bound of the tracking error, as a function of the sampling frequency and perturbation bound, has not been presented. This issue is addressed by the discrete-time domain stability analysis of the incremental control in this paper, which allows convenient yet realistic performance assessment and parameter tuning before performing real-world flight tests. Another challenge faced by the incremental control is that its stability criterion can be violated in severe aircraft fault scenarios, such as the control reversal. Therefore, this paper proposes a discrete-time control-direction-based incremental sliding mode control, denoted as D-INDI-SMC, which has broader applicability than the state-of-the-art incremental control methods. The robustness of D-INDI-SMC against control reversal, sensing errors, model uncertainties, actuator faults, and structural damage has been theoretically proved and numerically demonstrated.

Nomenclature

m_c	=	total mass, kg
A_x, A_y, A_z	=	specific force projected to the body frame, m/s^2
u, v, w	=	airspeed projected to the body frame, m/s
α, β	=	angle of attack, sideslip angle, rad
ρ_a	=	the air density, kg/m^3
S	=	wing surface area, m/s^2
$\bar{c}, b$	=	mean aerodynamic chord and wing span, m
V	=	airspeed, m/s
Ma	=	Mach number
C_x	=	force coefficient in the x direction
C_y	=	force coefficient in the y direction
$I_{xx}, I_{yy}, I_{zz}, I_{xz}$	=	second moments of inertia, kg·m^2
$\bar{q}$	=	dynamic pressure, Pa
ϕ, θ, ψ	=	Euler angles, rad
p, q, r	=	roll, pitch, and yaw rates, rad/s
$\delta_a, \delta_e, \delta_r$	=	deflections of the aileron, elevator, and rudder, rad
$\rho(X)$	=	the spectral radius of a matrix $X \in \mathbb{R}^{n \times n}$

---

*Assistant Professor, Shool of Aerospace Science and Technology, Xidian University, Xi'an, 710126, China. & Visiting Scholar, Faculty of Aerospace Engineering, Delft University of Technology, The Netherlands. jchang@xidian.edu.cn; J.Chang-2@tudelft.nl.

†Associate Professor, Faculty of Aerospace Engineering, Delft University of Technology; Kluyverweg 1, 2629HS, Delft, The Netherlands. R.DeBreuker@tudelft.nl, AIAA Associate Fellow.

‡Assistant Professor, Faculty of Aerospace Engineering, Delft University of Technology; Kluyverweg 1, 2629HS, Delft, The Netherlands. X.Wang-6@tudelft.nl, Member AIAA.

I. Introduction

THE aerospace industry has attracted much attention from different scientific and engineering communities such as control engineering, mechanical engineering, and computer science for resolving numerous challenges in guidance, navigation, and control (GNC) systems. Modern aircraft can be affected by multiple uncertainties (parametric and nonparametric perturbations), external disturbances (turbulence, wind gust), and new fault modes [1]. Highly nonlinear characteristics, structural damage, actuator/sensor fault, and complex coupling effects, combined with unknown multiple uncertainties cause a considerable challenge in designing a reliable control system for modern aerospace systems.

The existing fault tolerant flight control (FTFC) methods can be classified into four groups: robust control approaches against pre-specified faults (robust $\mathcal{H}_\infty$ control), selection of a new pre-computed control law (multiple-model approaches), synthesizing a new control strategy online (pseudo-inverse method, model predictive control, adaptive control, sliding mode control), and using dynamic control allocation. The development and current status of FTFC and its application in aerospace systems have been reviewed in [2, 3]. Many advanced FTFC techniques need a complicated online model identification strategy to robustly resist the sudden properties changes of the aircraft. Furthermore, there are several challenges in both theoretical and practical implementations: 1) the real-time implementation of a fault-tolerant control system; 2) the safety, reliability, and reconfigurability analysis and assessment; 3) switching mechanisms within the reconfiguration architecture. The strong motivation for the innovative technology development of any fault-tolerant control methods is the transfer of knowledge in the aerospace arena which can generate economic added value and benefits to society. However, only a few of the modern control methods have been applied to the real-world aerospace industry. Most of them do not provide clear and formalized parameter tuning guidelines and lack feasibility analysis and real-world requirement specifications.

A sensor-based control framework named incremental control, which includes incremental nonlinear dynamic inversion (INDI) and incremental backstepping (IBS) has been developed for fault-tolerant control problems [4–6]. This sensor-based control framework can provide high-performance nonlinear control without requiring a detailed model of the controlled vehicle, which is promising for the highly uncertain aerospace systems. Recent developments in incremental control have highlighted the need for closed-loop analysis to identify and understand the effects of perturbations in closed-loop characteristics. Using transfer functions, the effects of the model uncertainties on the single-input single-output (SISO) aircraft attitude dynamics using both classical and incremental backstepping controllers are assessed in [7, 8]. Lyapunov-based stability analyses for multi-input multi-output (MIMO) nonlinear systems using incremental control in the presence of model uncertainties, sudden actuator faults, and structural damage are presented in [9]. Thanks to the inherent robustness of INDI, it can passively resist faults and uncertainties that satisfy the conditions given in [9, 10]. To further enhance the applicability of INDI, it has been hybridized with sliding modes control (SMC) for matched disturbances and faults [10, 11]. The effectiveness and easy implementation of INDI-SMC have been demonstrated by real-world quadrotor flight tests [11].

Although extensive research has been carried out on incremental control, there still exist many open research questions. For example, what are the impacts of sensing error on the closed-loop characteristics? How to deal with control reversal? To address these questions, this paper focuses on the design and stability analysis of incremental fault-tolerant flight control in the discrete-time domain considering sensing errors, control reversal, model uncertainties, actuator faults, and structural damage. The impacts of various sources of uncertainty on the ultimate bound of the tracking errors are explicitly quantified. To deal with control reversal, a discrete-time control direction-based incremental sliding mode control, denoted as D-INDI-SMC, is proposed. Its stability and robustness are proved theoretically and are verified by numerical simulations.

The rest of this paper is structured as follows. The discrete-time stability analysis of INDI is discussed in Sec. II. Section III deals with D-INDI-SMC design for MIMO system. A model of the rigid-body aircraft is given in Sec. IV. Finally, the numerical simulation setup is explained, followed by the results and discussions in Sec. V.

II. Discrete-time Stability Analysis for Nonlinear Incremental Control

A. Preliminary

Consider an MIMO nonlinear control-affine system described in continuous time-domain by

$$\dot{x} = f(x) + G(x)u, \quad y = h(x) \tag{1}$$

where $x \in \mathbb{R}^n$ is the state of the system, $u \in \mathbb{R}^m$ is the system input, $y \in \mathbb{R}^m$ is the system output, $f : \mathbb{R}^n \to \mathbb{R}^n$, $G : \mathbb{R}^n \to \mathbb{R}^{n \times m}$ and $h : \mathbb{R}^n \to \mathbb{R}^m$ are continuous functions. Denote the elements of h as $h_i, i = 1, \ldots, m$, and the

j-th column vector of the matrix function $\boldsymbol{G}$ as $\boldsymbol{g}_j$, $j = 1, \ldots, m$. The Lie derivatives of h_i with respect to $\boldsymbol{f}$ and $\boldsymbol{g}_j$ is defined as [10]

$$\mathcal{L}_f^{\rho_i} h_i = \frac{\partial (\mathcal{L}_f^{(\rho_i-1)} h_i)}{\partial \boldsymbol{x}} \boldsymbol{f}, \quad \mathcal{L}_{g_j} \mathcal{L}_f^{(\rho_i-1)} h_i = \frac{\partial (\mathcal{L}_f^{(\rho_i-1)} h_i)}{\partial \boldsymbol{x}} \boldsymbol{g}_j \tag{2}$$

where ρ_i represents the relative degree for the i-th control channel. Assume $\rho_1 + \rho_2 + \cdots + \rho_m = n$. Using the Lie derivatives, the input-output mapping of the system is given by

$$\boldsymbol{y}^{(\rho)} = \boldsymbol{\alpha}(\boldsymbol{x}) + \mathcal{B}(\boldsymbol{x})\boldsymbol{u} \tag{3}$$

where $\mathcal{B}(\boldsymbol{x}) \in \mathbb{R}^{m \times m}$, $\boldsymbol{\alpha}(\boldsymbol{x}) \in \mathbb{R}^{m \times 1}$, $\boldsymbol{\rho} = [\rho_1, \rho_2, \ldots, \rho_m]^\mathsf{T}$ and

$$\boldsymbol{\alpha}(\boldsymbol{x}) = \begin{bmatrix} \mathcal{L}_f^{\rho_1} h_1 \\ \mathcal{L}_f^{\rho_2} h_2 \\ \vdots \\ \mathcal{L}_f^{\rho_m} h_m \end{bmatrix}, \quad \mathcal{B}(\boldsymbol{x}) = \begin{bmatrix} \mathcal{L}_{g_1} \mathcal{L}_f^{(\rho_1-1)} h_1 & \mathcal{L}_{g_2} \mathcal{L}_f^{(\rho_1-1)} h_1 & \cdots & \mathcal{L}_{g_m} \mathcal{L}_f^{(\rho_1-1)} h_1 \\ \vdots & \vdots & \ddots & \vdots \\ \mathcal{L}_{g_1} \mathcal{L}_f^{(\rho_m-1)} h_m & \mathcal{L}_{g_2} \mathcal{L}_f^{(\rho_m-1)} h_m & \cdots & \mathcal{L}_{g_m} \mathcal{L}_f^{(\rho_m-1)} h_m \end{bmatrix} \tag{4}$$

Define external state as $\boldsymbol{\xi}^\mathsf{T} = [\boldsymbol{\xi}_1^\mathsf{T}, \boldsymbol{\xi}_2^\mathsf{T}, \ldots, \boldsymbol{\xi}_m^\mathsf{T}]$, $\boldsymbol{\xi}_i = [h_i, \mathcal{L}_f h_i, \ldots, \mathcal{L}_f^{(\rho_i-1)} h_i]^\mathsf{T}$, $i = 1, \ldots, m$. The state vector for internal dynamics of the system is indicated as $\boldsymbol{\eta}$. Apply the change of coordinates $\boldsymbol{z} \mapsto T(\boldsymbol{x})$, then a new state representation $\boldsymbol{z}^\mathsf{T} = [\boldsymbol{\eta}^\mathsf{T}, \boldsymbol{\xi}^\mathsf{T}]$ is created. The nonlinear system in Eq. (1) can be transformed into a canonical form as

$$\begin{cases} \dot{\boldsymbol{\eta}} = \boldsymbol{f}_{\text{in}}(\boldsymbol{\eta}, \boldsymbol{\xi}) \\ \dot{\boldsymbol{\xi}} = \boldsymbol{A}_c \boldsymbol{\xi} + \boldsymbol{B}_c [\boldsymbol{\alpha}(\boldsymbol{x}) + \mathcal{B}(\boldsymbol{x})\boldsymbol{u}] \\ \boldsymbol{y} = \boldsymbol{C}_c \boldsymbol{\xi} \end{cases} \tag{5}$$

Taking the first-order Taylor series expansion of Eq. (3) at $t - h$ with $\boldsymbol{x}_0 = \boldsymbol{x}(t - h)$, $\boldsymbol{u}_0 = \boldsymbol{u}(t - h)$, where h is one sampling interval, we obtain the incremental dynamics

$$\begin{aligned} \boldsymbol{y}^{(\rho)} &= \boldsymbol{y}^{(\rho)}\Big|_0 + \frac{\partial [\boldsymbol{\alpha}(\boldsymbol{x}) + \mathcal{B}(\boldsymbol{x})\boldsymbol{u}]}{\partial \boldsymbol{x}}\Big|_0 \Delta \boldsymbol{x} + \mathcal{B}(\boldsymbol{x})\Big|_0 \Delta \boldsymbol{u} + \boldsymbol{R}_1(\boldsymbol{x}, \boldsymbol{u}, h) \\ &\triangleq \boldsymbol{y}_0^{(\rho)} + \mathcal{A}_0(\boldsymbol{x}) \triangle \boldsymbol{x} + \mathcal{B}_0(\boldsymbol{x}) \triangle \boldsymbol{u} + \boldsymbol{R}_1(\boldsymbol{x}, \boldsymbol{u}, h) \end{aligned} \tag{6}$$

where $\boldsymbol{R}_1$ is the expansion remainder, whose Lagrange form is

$$\boldsymbol{R}_1(\boldsymbol{x}, \boldsymbol{u}, h) = \frac{1}{2} \frac{\partial^2 [\boldsymbol{\alpha}(\boldsymbol{x}) + \mathcal{B}(\boldsymbol{x})\boldsymbol{u}]}{\partial^2 \boldsymbol{x}}\Big|_m \Delta \boldsymbol{x}^2 + \frac{\partial^2 [\boldsymbol{\alpha}(\boldsymbol{x}) + \mathcal{B}(\boldsymbol{x})\boldsymbol{u}]}{\partial \boldsymbol{x} \partial \boldsymbol{u}}\Big|_m \Delta \boldsymbol{x} \Delta \boldsymbol{u} \tag{7}$$

where $(\cdot)|_m$ means evaluating $(\cdot)$ at $(\boldsymbol{x}_m, \boldsymbol{u}_m)$ where $\boldsymbol{x}_m \in [\boldsymbol{x}(t - h), \boldsymbol{x}(t)]$ and $\boldsymbol{u}_m \in [\boldsymbol{u}(t - h), \boldsymbol{u}(t)]$. $\triangle \boldsymbol{x}$ and $\triangle \boldsymbol{u}$ represent the state and control increments in one sampling interval h.

The control object is to make the output $\boldsymbol{y}$ track a reference signal $\boldsymbol{y}_r = [y_{r,1}, y_{r,2}, \ldots, y_{r,m}]^\mathsf{T}$. Denote the reference state vector as $\boldsymbol{r} = [\boldsymbol{r}_1, \boldsymbol{r}_2, \ldots, \boldsymbol{r}_m]^\mathsf{T}$ with $\boldsymbol{r}_i = [y_{r,i}, y_{r,i}^{(1)}, \ldots, y_{r,i}^{(\rho_i-1)}]$, $i = 1, \ldots, m$. Define the tracking error vector as $\boldsymbol{e} = \boldsymbol{\xi} - \boldsymbol{r}$. Substituting Eq. (6) into Eq. (5), the error dynamics are given by

$$\dot{\boldsymbol{e}} = \boldsymbol{A}_c \boldsymbol{e} + \boldsymbol{B}_c \left(\boldsymbol{y}_0^{(\rho)} + \mathcal{B}_0(\boldsymbol{x}) \Delta \boldsymbol{u} + \mathcal{A}_0(\boldsymbol{x}) \Delta \boldsymbol{x} + \boldsymbol{R}_1(\boldsymbol{x}, \boldsymbol{u}, h) - \boldsymbol{y}_r^{(\rho)} \right) \tag{8}$$

where $\boldsymbol{y}_r^{(\rho)} = [y_{r,1}^{\rho_1}, y_{r,2}^{\rho_2}, \ldots, y_{r,m}^{\rho_m}]^\mathsf{T}$.

The incremental control law for stabilizing the error dynamics is then designed as

$$\Delta \boldsymbol{u}_{\text{indi}} = \hat{\mathcal{B}}_0^{-1}(\boldsymbol{x}) \left(\boldsymbol{v}_c - \hat{\boldsymbol{y}}_0^{(\rho)} \right), \quad \boldsymbol{v}_c = -\boldsymbol{K}\boldsymbol{e} + \boldsymbol{y}_r^{(\rho)}, \quad \boldsymbol{u} = \boldsymbol{u}_0 + \Delta \boldsymbol{u}_{\text{indi}} \tag{9}$$

where $\boldsymbol{K} \in \mathbb{R}^{m \times n}$ is designed such that $\boldsymbol{A}_c - \boldsymbol{B}_c \boldsymbol{K}$ is Hurwitz; $\hat{\mathcal{B}}_0(\boldsymbol{x})$ is an estimation of $\mathcal{B}_0(\boldsymbol{x})$; $\hat{\boldsymbol{y}}_0^{(\rho)}$ is the measured or estimated signal of $\boldsymbol{y}_0^{(\rho)}$. Substituting Eq. (9) into Eq. (8), we have

$$\dot{\boldsymbol{e}} = (\boldsymbol{A}_c - \boldsymbol{B}_c \boldsymbol{K})\boldsymbol{e} + \boldsymbol{B}_c \underbrace{\left[(\mathcal{B}_0(\boldsymbol{x}) \hat{\mathcal{B}}_0^{-1}(\boldsymbol{x}) - \boldsymbol{I}) \left(\boldsymbol{v}_c - \hat{\boldsymbol{y}}_0^{(\rho)} \right) + \tilde{\boldsymbol{y}}_0^{(\rho)} + \boldsymbol{\delta}(\boldsymbol{z}, h) \right]}_{\boldsymbol{\varepsilon}_{\text{indi}}} \tag{10}$$

$$\triangleq (\boldsymbol{A}_c - \boldsymbol{B}_c \boldsymbol{K})\boldsymbol{e} + \boldsymbol{B}_c \boldsymbol{\varepsilon}_{\text{indi}}$$

3

with

$$\tilde{\boldsymbol{y}}_0^{(\rho)} = \boldsymbol{y}_0^{(\rho)} - \hat{\boldsymbol{y}}_0^{(\rho)}, \quad \boldsymbol{\delta}(z, h) = [\mathcal{A}_0(\boldsymbol{x})\Delta\boldsymbol{x} + \boldsymbol{R}_1(\boldsymbol{x}, \boldsymbol{u}, h)]\Big|_{z=T(\boldsymbol{x}_0), \boldsymbol{u}=\boldsymbol{u}_0+\Delta\boldsymbol{u}_{\text{indi}}} \tag{11}$$

Assumption 1 *[10] The measurement or estimation error of $\boldsymbol{y}_0^{(\rho)}$ is bounded; i.e., $\|\tilde{\boldsymbol{y}}_0^{(\rho)}\| \leq \bar{\delta}_y$.*

Assumption 2 *[9] The term $\boldsymbol{\delta}(z, h)$ in Eq. (10), which contains the closed-loop values of the expansion remainder $\boldsymbol{R}_1$ and $\mathcal{A}_0(\boldsymbol{x})\Delta\boldsymbol{x}$, is bounded; i.e., $\|\boldsymbol{\delta}(z, h)\| \leq \bar{\delta}_z$.*

Remark 1 Assumption 1 is commonly used in observer-based controllers. The bounded estimation error is the basic requirement for the design of an estimator. Assumption 2 is commonly made in many references [6, 10] for incremental controller design since the linearization error is generally bounded. Moreover, based on Eq. (11), increasing the sampling frequency can reduce the value of $\|\boldsymbol{\delta}(z, h)\|$. Therefore, Assumptions 1 and 2 are reasonable.

Equation (10) gives the closed-loop system dynamics under the nominal INDI control. It can also be observed from Eq. (10) that the perturbation terms $\boldsymbol{\varepsilon}_{\text{indi}}$ determines the stability and convergent performance. The stability of system in Eq. (5) under INDI control has been discussed in [9]. The following lemma has been proved.

Lemma 1 *[9] If $\|\boldsymbol{\varepsilon}_{indi}\| \leq \delta_\varepsilon$ is satisfied for all $z \in \mathbb{R}^n$, and $\dot{\boldsymbol{\eta}} = \boldsymbol{f}_{in}(\boldsymbol{\eta}, \boldsymbol{\xi})$ is input-to-state stable, then the state z of Eq. (5) is globally ultimately bounded by a class $\mathcal{K}$ function of δ_ε.*

If $\boldsymbol{\varepsilon}_{\text{indi}}$ is bounded, then $\boldsymbol{e}$ is globally uniformly ultimately bounded. In the literature, the state variation-related terms and Taylor expansion reminders are directly omitted in the some of the INDI derivations [6, 7, 12, 13]. However, the statement for supporting the term omission (the $\triangle\boldsymbol{x}$ related term is smaller than the $\triangle\boldsymbol{u}$ related term when the sampling frequency is high) is not mathematically rigorous. A continuous-time Lyapunov-based stability analysis without using the term omission has been presented in [9]. However, the sensing error $\tilde{\boldsymbol{y}}_0^{(\rho)}$ is not considered in [9]. Furthermore, the assumption of sufficiently high sampling frequency is used in [9] without presenting an explicit criterion for how high the sampling frequency should be. These two issues are considered in a discrete-time stability analysis for the INDI control in Sec. II.B.

B. Stability and Robustness Analysis

The stability and robustness of the INDI control in the presence of model uncertainties and sensing errors will be analyzed in this subsection. Analogous to the derivation in [10], using the fact that $\boldsymbol{y}^{(\rho)} = \boldsymbol{v}_c + \boldsymbol{\varepsilon}_{\text{indi}}$, the residual cancellation error of INDI can be rewritten as

$$\begin{aligned}
\boldsymbol{\varepsilon}_{\text{indi}} &= \left(\boldsymbol{I} - \mathcal{B}_0(\boldsymbol{x})\hat{\mathcal{B}}_0^{-1}(\boldsymbol{x})\right)\boldsymbol{\varepsilon}_{\text{indi},0} + (\mathcal{B}_0(\boldsymbol{x})\hat{\mathcal{B}}_0^{-1}(\boldsymbol{x}) - \boldsymbol{I})\Delta\boldsymbol{v}_c + \mathcal{B}_0(\boldsymbol{x})\hat{\mathcal{B}}_0^{-1}(\boldsymbol{x})\tilde{\boldsymbol{y}}_0^{(\rho)} + \boldsymbol{\delta}(z, h) \\
&= \boldsymbol{\Phi}_0(\boldsymbol{x})\boldsymbol{\varepsilon}_{\text{indi},0} - \boldsymbol{\Phi}_0(\boldsymbol{x})\Delta\boldsymbol{v}_c + (\boldsymbol{I} - \boldsymbol{\Phi}_0(\boldsymbol{x}))\tilde{\boldsymbol{y}}_0^{(\rho)} + \boldsymbol{\delta}(z, h)
\end{aligned} \tag{12}$$

with $\boldsymbol{\Phi}_0(\boldsymbol{x}) = \boldsymbol{I} - \mathcal{B}_0(\boldsymbol{x})\hat{\mathcal{B}}_0^{-1}(\boldsymbol{x})$. Using $\boldsymbol{\Phi}(k), \Delta\boldsymbol{v}_c(k), \tilde{\boldsymbol{y}}_0^{(\rho)}(k), \boldsymbol{\delta}(k)$ to represent the value of $\boldsymbol{\Phi}_0(\boldsymbol{x}), \Delta\boldsymbol{v}_c, \tilde{\boldsymbol{y}}_0^{(\rho)}$, $\boldsymbol{\delta}(z, h)$ at $t = kh$ respectively, then the residual error at the $(k + 1)$-th time step is written in a recursive way as

$$\boldsymbol{\varepsilon}_{\text{indi}}(k + 1) = \boldsymbol{\Phi}(k)\boldsymbol{\varepsilon}_{\text{indi}}(k) - \boldsymbol{\Phi}(k)\Delta\boldsymbol{v}_c(k) + (\boldsymbol{I} - \boldsymbol{\Phi}(k))\tilde{\boldsymbol{y}}_0^{(\rho)}(k) + \boldsymbol{\delta}(k) \tag{13}$$

Note that $\boldsymbol{v}_c$ is designed to be continuous in time, thus $\lim_{h \to 0} \|\Delta\boldsymbol{v}_c(k)\| = 0$. Therefore, under sufficiently high sampling frequency, $\Delta\boldsymbol{v}_c(k)$ is bounded as $\|\Delta\boldsymbol{v}_c(k)\| \leq \bar{\Delta}_{\boldsymbol{v}_c}$. If $\boldsymbol{\Phi}(k)$ satisfies $\|\boldsymbol{\Phi}(k)\| \leq \bar{b} < 1$, then the residual error of the controller given by Eq. (12) is further derived as

$$\|\boldsymbol{\varepsilon}_{\text{indi}}(k + 1)\| \leq \bar{b}^k\|\boldsymbol{\varepsilon}_{\text{indi}}(0)\| + \bar{\Delta}_{\boldsymbol{v}_c}\frac{\bar{b} - \bar{b}^{k+1}}{1 - \bar{b}} + \bar{\delta}_z\frac{1 - \bar{b}^k}{1 - \bar{b}} + \bar{\delta}_y\frac{(\bar{b} - \bar{b}^k)(1 + \bar{b})}{1 - \bar{b}} \tag{14}$$

which follows

$$\lim_{k \to \infty} \|\boldsymbol{\varepsilon}_{\text{indi}}\| \leq \frac{\bar{\Delta}_{\boldsymbol{v}_c}\bar{b}}{1 - \bar{b}} + \frac{\bar{\delta}_z}{1 - \bar{b}} + \frac{\bar{\delta}_y\bar{b}(1 + \bar{b})}{1 - \bar{b}} \tag{15}$$

which means $\boldsymbol{\varepsilon}_{\text{indi}}$ is ultimately bounded. Using Euler's forward approximation, the discrete error dynamics of (9) are written as

$$\boldsymbol{e}(k + 1) = (\boldsymbol{I} + h(\boldsymbol{A}_c - \boldsymbol{B}_c\boldsymbol{K}))\boldsymbol{e}(k) + h\boldsymbol{B}_c\boldsymbol{\varepsilon}_{\text{indi}}(k) \tag{16}$$

4

Additionally, since $(A_c - B_c K)$ is Hurwtiz, then $\|I + h(A_c - B_c K)\| \leq \bar{\lambda} < 1$. Application of this property and the Eq. (14) to Eq. (16) yields the bound

$$\|e(k+1)\| \leq \bar{\lambda}^k \|e(0)\| + \frac{h(1 - \bar{\lambda}^k)}{1 - \bar{\lambda}} \left(\bar{b}^{k-1} \|\varepsilon_{\text{indi}}(0)\| + \frac{(1 - \bar{b}^{k-1})(\bar{\Delta}_{v_c} \bar{b} + \bar{\delta}_z) + \bar{\delta}_y(\bar{b} - \bar{b}^{k-1})(1 + \bar{b})}{1 - \bar{b}} \right) \quad (17)$$

After taking into account $\bar{\lambda} < 1, \bar{b} < 1$, the following can be easily obtained

$$\lim_{k \to \infty} \|e(k+1)\| \leq \frac{h\bar{\Delta}_{v_c} \bar{b} + h\bar{\delta}_z + h\bar{\delta}_y \bar{b}(1 + \bar{b})}{(1 - \bar{b})(1 - \bar{\lambda})} \quad (18)$$

Therefore, the system under INDI control (Eq. (9)) is globally uniformly ultimately bounded.

Remark 2 In essential, Eq. (18) presents the expression for the ultimate bound of the tracking error, which is a function of the sampling interval and the model uncertain metrics. In the literature, the term $y_0^{(\rho)}$ is often directly assumed to be known [6, 9, 13]. Although in observer-based control methods, the estimate error term $\tilde{y}_0^{(\rho)}$ is often dropped out for the convenience of control design [7, 9], it should be kept in the closed-loop system equations for rigorously analyzing stability and robustness [14]. By contrast, the impacts of $\tilde{y}_0^{(\rho)}$ on the closed-loop dynamics have been considered in the preceding analysis, and will be further assessed in Section III .

III. Discrete-time Incremental Sliding Mode Control

The presented INDI control has shown promising inherent robustness to the regular perturbations without using any robust or adaptive control technique [7, 10]. Based on the preceding analysis, the stability of INDI control is constrained by $\|\Phi_0(x)\| < 1$. However, in reality, this constrain can be violated in severe faulty circumstances. For example, the elements of the control effectiveness matrix have the possibility to switch their signs [15]. Regarding the aircraft attitude dynamics, the control effectiveness matrix $\mathcal{B}(x)$ is normally diagonally dominant. If the diagonal entries of $\mathcal{B}(x)$ and $\hat{\mathcal{B}}(x)$ have opposite signs, the condition $\|\Phi_0(x)\| < 1$ would be violated. As a consequence, the stability of the INDI control cannot be theoretically guaranteed in this scenario. To expand the applicability of INDI, a discrete-time control direction-based incremental sliding mode control, denoted as D-INDI-SMC, will be proposed in this section.

The uncertainties in $\mathcal{B}(x)$ caused by actuator faults and damage are mainly resulted in degradation on the diagonal entry. Consider the model of flight dynamics in [10], the incremental input-output mapping of this kind of system can be rewritten in the following form

$$y^{(\rho)} = y_0^{(\rho)} + \bar{\mathcal{B}}_0(x)\Lambda\Delta u + \mathcal{A}_0(x)\triangle x + R_1(x, u, h) \quad (19)$$

where $\bar{\mathcal{B}}_0(x) \in \mathbb{R}^{m \times m}$ is the known nominal control matrix; $\Lambda \in \mathbb{R}^{m \times m}$ is a diagonal and unknown time-varying control degradation matrix and $\Lambda = \text{diag}\{w_1, w_2, \ldots, w_m\}$. There is a common precondition for the control effectiveness uncertainties in aircraft fault tolerant flight control. It is widely assumed that the control effectiveness degradation satisfies $\underline{w} < |w_m| < 1$ [15–17]. Here, we consider that the control effectiveness could also be bigger than the nominal value in practice. Thus, we assume that the uncertainties in the control matrix satisfy $\underline{w} < |w_m| < 2$ for a border practical scenario.

Using Eq. (19), the error dynamics in (8) becomes

$$\dot{e} = A_c e + B_c \left(y_0^{(\rho)} + \bar{\mathcal{B}}_0(x)\Lambda\Delta u + \mathcal{A}_0(x)\Delta x + R_1(x, u, h) - y_r^{(\rho)} \right) \quad (20)$$

and can be discretized using Euler's forward approximation as

$$e(k+1) = [I + hA_c] e(k) + hB_c \left(y_0^{(\rho)}(k) + \bar{\mathcal{B}}_0(k)\Lambda(k)\Delta u(k) + \mathcal{A}_0(k)\Delta x(k) + R_1(k) - y_r^{(\rho)}(k) \right) \quad (21)$$

Assumption 3 *The signs of the diagonal elements of the matrix Λ are known.*

Lemma 2 *[18] If the matrices $X_1 \in \mathbb{R}^{n \times n}$ and $X_2 \in \mathbb{R}^{n \times n}$ are similar, then they have the same eigenvalues and ranks.*

The control structure of control direction-based discrete-time incremental sliding mode control is proposed as

$$\Delta \boldsymbol{u}_{\text{indi-s}}(k) = \text{sgn}(\boldsymbol{\Lambda}(k))\bar{\boldsymbol{\mathcal{B}}}_0^{-1}(k)\left(\boldsymbol{v}_c(k) + \boldsymbol{v}_s(k) - \hat{\boldsymbol{y}}_0^{(\rho)}(k)\right), \tag{22}$$

where $\text{sgn}(\boldsymbol{\Lambda}(k)) = \text{diag}\{\text{sign}(w_1), \text{sign}(w_2), \ldots, \text{sign}(w_m)\}$, $\boldsymbol{v}_c(k) = -\boldsymbol{K}\boldsymbol{e}(k) + \boldsymbol{y}_r^{(\rho)}(k)$ is the INDI virtual control for stabilizing the unperturbed system, which is identical to the $\boldsymbol{v}_c$ in Eq. (9). The term $\boldsymbol{v}_s$ is designed for perturbation compensations.

Design the discrete sliding variable $\boldsymbol{\sigma}(\boldsymbol{e}) : \mathbb{R}^n \to \mathbb{R}^m$ as

$$\boldsymbol{\sigma}(k) = \boldsymbol{S}\boldsymbol{e}(k) - \boldsymbol{S}\boldsymbol{e}(0) + \boldsymbol{E}_I(k), \quad \boldsymbol{E}_I(k) = \boldsymbol{E}_I(k-1) + \boldsymbol{K}_e \boldsymbol{e}(k-1) \tag{23}$$

where $\boldsymbol{K}_e = -h\boldsymbol{S}(\boldsymbol{A}_c - \boldsymbol{B}_c\boldsymbol{K}) = \text{diag}\{[K_{i,e}, 0, \cdots, 0]\}$, $\boldsymbol{S} = \text{diag}\{\boldsymbol{S}_i\}$, $\boldsymbol{S}_i = [K_{i,1}, K_{i,\rho_i-1}, 1]$. Consider the motions on the sliding surface, i.e., $\boldsymbol{\sigma}(k+1) = \boldsymbol{\sigma}(k) = 0$, then using Eqs. (21) and (23), the following equations are derived:

$$\begin{cases} \boldsymbol{\sigma}(k+1) = \boldsymbol{S}\left[\boldsymbol{I} + h\boldsymbol{A}_c\right]\boldsymbol{e}(k) - \boldsymbol{S}\boldsymbol{e}(0) + \boldsymbol{E}_I(k+1) \\ \qquad + h\boldsymbol{S}\boldsymbol{B}_c\left(\boldsymbol{y}_0^{(\rho)}(k) + \bar{\boldsymbol{\mathcal{B}}}_0(k)\boldsymbol{\Lambda}(k)\Delta\boldsymbol{u}(k) + \mathcal{A}_0(k)\Delta\boldsymbol{x}(k) + \boldsymbol{R}_1(k) - \boldsymbol{y}_r^{(\rho)}(k)\right) = 0 \\ \boldsymbol{\sigma}(k) = \boldsymbol{S}\boldsymbol{e}(k) - \boldsymbol{S}\boldsymbol{e}(0) + \boldsymbol{E}_I(k) = 0, \quad \boldsymbol{E}_I(k+1) = \boldsymbol{E}_I(k) + \boldsymbol{K}_e\boldsymbol{e}(k) \end{cases} \tag{24}$$

Using Eq. (24), the equivalent control is calculated by:

$$\Delta\boldsymbol{u}_{\text{eq}}(k) = \boldsymbol{\Lambda}^{-1}(k)\bar{\boldsymbol{\mathcal{B}}}_0^{-1}(k)(\boldsymbol{y}_r^{(\rho)}(k) - \boldsymbol{K}\boldsymbol{e}(k) - \boldsymbol{y}_0^{(\rho)}(k) - \boldsymbol{\delta}_s(k)) \tag{25}$$

where $\boldsymbol{\delta}_s(k) = \left[\mathcal{A}_0(\boldsymbol{x})\Delta\boldsymbol{x} + \boldsymbol{R}_1(\boldsymbol{x}, \boldsymbol{u}, h)\right]\Big|_{\boldsymbol{z}=\boldsymbol{T}(\boldsymbol{x}_0(k)), \boldsymbol{u}=\boldsymbol{u}_0(k)+\Delta\boldsymbol{u}_{\text{indi-s}}(k)}$.

Substituting Eq. (25) into Eq. (21), the ideal sliding mode dynamic equation results in:

$$\boldsymbol{e}(k+1) = \left[\boldsymbol{I} + h(\boldsymbol{A}_c - \boldsymbol{B}_c\boldsymbol{K})\right]\boldsymbol{e}(k) \tag{26}$$

Equation (26) indicates that on the sliding surface, the desired error dynamics are achieved, which ensure $\boldsymbol{e}$ converges to zero and $\boldsymbol{\xi} \to \boldsymbol{r}$. To compensate for uncertainties and disturbances, the sliding mode virtual control $\boldsymbol{v}_s$ is designed as

$$\boldsymbol{v}_s(k) = -\boldsymbol{K}_s\text{sgn}(\boldsymbol{\sigma}(k))^{\gamma} = -[K_{s,1}|\sigma_1(k)|^{\gamma_1}\text{sign}(\sigma_1(k)), \ldots, K_{s,m}|\sigma_m(k)|^{\gamma_m}\text{sign}(\sigma_m(k))]^{\mathsf{T}} \tag{27}$$

where $K_{s,i} > 0$, $\gamma_i \in (0, 1)$.

Theorem 1 *If Assumptions 1-3 are satisfied, $\boldsymbol{f}_{in}(\boldsymbol{\eta}, \boldsymbol{\xi})$ is continuously differentiable and globally Lipschitz in $(\boldsymbol{\eta}, \boldsymbol{\xi})$, and the origin of $\dot{\boldsymbol{\eta}} = \boldsymbol{f}_{in}(\boldsymbol{\eta}, \boldsymbol{0})$ is globally exponentially stable, then using the proposed control law in Eq. (22), the tracking error $\boldsymbol{e}$ in Eq. (20) converges to an arbitrary small bound, while the internal state $\boldsymbol{\eta}$ in Eq. (5) is globally ultimately bounded.*

Proof 1 *: Substituting Eq. (22) and Eq. (21) into Eq. (23) yields*

$$\begin{aligned} \boldsymbol{\sigma}(k+1) =& \boldsymbol{S}\boldsymbol{e}(k+1) - \boldsymbol{S}\boldsymbol{e}(0) + \boldsymbol{E}_I(k) + \boldsymbol{K}_e\boldsymbol{e}(k) \\ =& \boldsymbol{S}\left[\boldsymbol{I} + h\boldsymbol{A}_c\right]\boldsymbol{e}(k) - \boldsymbol{S}\boldsymbol{e}(0) + \boldsymbol{E}_I(k) + \boldsymbol{K}_e\boldsymbol{e}(k) \\ &+ h\boldsymbol{S}\boldsymbol{B}_c\left(\boldsymbol{y}_0^{(\rho)}(k) + \bar{\boldsymbol{\mathcal{B}}}_0(k)\boldsymbol{\Lambda}(k)sgn(\boldsymbol{\Lambda}(k))\bar{\boldsymbol{\mathcal{B}}}_0^{-1}(k)(\boldsymbol{v}_c(k) - \hat{\boldsymbol{y}}_0^{(\rho)}(k) + \boldsymbol{v}_s(k)) + \boldsymbol{\delta}_s(k) - \boldsymbol{y}_r^{(\rho)}(k)\right) \\ =& \boldsymbol{\sigma}(k) - h\boldsymbol{S}\boldsymbol{B}_c\boldsymbol{K}_s sgn(\boldsymbol{\sigma}(k))^{\gamma} \\ &+ h\boldsymbol{S}\boldsymbol{B}_c\left(-\underbrace{(\boldsymbol{I} - \bar{\boldsymbol{\mathcal{B}}}_0(k)|\boldsymbol{\Lambda}(k)|\bar{\boldsymbol{\mathcal{B}}}_0^{-1}(k))}_{\boldsymbol{\Phi}_s(k)}(\boldsymbol{v}_c(k) + \boldsymbol{v}_s(k) - \boldsymbol{y}_0^{(\rho)}(k)) + \underbrace{\bar{\boldsymbol{\mathcal{B}}}_0(k)|\boldsymbol{\Lambda}(k)|\bar{\boldsymbol{\mathcal{B}}}_0^{-1}(k)\tilde{\boldsymbol{y}}_0^{(\rho)}(k) + \boldsymbol{\delta}_s(k)}_{\tilde{\boldsymbol{\Delta}}_s(k)}\right) \\ =& \boldsymbol{\sigma}(k) + h\boldsymbol{S}\boldsymbol{B}_c\left(-\boldsymbol{K}_s sgn(\boldsymbol{\sigma}(k))^{\gamma} - \boldsymbol{\Phi}_s(k)(\boldsymbol{v}_c(k) + \boldsymbol{v}_s(k) - \boldsymbol{y}_0^{(\rho)}(k)) - \tilde{\boldsymbol{\Delta}}_s(k)\right) \end{aligned} \tag{28}$$

where $|\boldsymbol{\Lambda}| = diag\{|w_1|, |w_2|, \ldots, |w_m|\}$.

6

According to Corollary 2, we conclude that the eigenvalues of $\boldsymbol{\Phi}_s(k)$ are $eig\{\boldsymbol{I} - |\boldsymbol{\Lambda}|\}$. With Assumption 1 and 2, it follows

$$\|\tilde{\boldsymbol{\Delta}}_s(k)\| \leq (\rho(\boldsymbol{\Lambda}) + \varepsilon)\bar{\delta}_y + \bar{\delta}_z, \quad 0 < \varepsilon \ll 1 \tag{29}$$

The following equation is established using the controller in Eq. (22)

$$\boldsymbol{y}^{(\rho)}(k) = \boldsymbol{v}_c(k) + \boldsymbol{v}_s(k) + \underbrace{\tilde{\boldsymbol{\Delta}}_s(k) - \boldsymbol{\Phi}_s(k)(\boldsymbol{v}_c(k) + \boldsymbol{v}_s(k) - \boldsymbol{y}_0^{(\rho)}(k))}_{\boldsymbol{\varepsilon}_{indi_s}(k)} \tag{30}$$

Therefore, analogous to Eq. (12), yielding

$$\boldsymbol{\varepsilon}_{indi_s}(k) = \boldsymbol{\Phi}_s(k)\boldsymbol{\varepsilon}_{indi_s}(k-1) - \boldsymbol{\Phi}_s(k)(\Delta\boldsymbol{v}_c(k) + \Delta\boldsymbol{v}_s(k)) + \tilde{\boldsymbol{\Delta}}_s(k) \tag{31}$$

According to [19], since both $\boldsymbol{v}_c(t)$ and $\boldsymbol{v}_s(t)$ are designed to be continuous in time, the incremental terms $\Delta\boldsymbol{v}_c(k), \Delta\boldsymbol{v}_s(k)$ are in the order of magnitude of $O(h^2)$. Using the assumption $\bar{w} < |w_i| < 2, i = 1, 2, \ldots, m$ in the system model Eq. (19), it obtains $\rho(\boldsymbol{I} - |\boldsymbol{\Lambda}|) < 1$. This yields $\rho(\boldsymbol{\Phi}_s(k)) < 1$ and $\boldsymbol{\varepsilon}_{indi_s}(k)$ is bounded, i.e., $\|\boldsymbol{\varepsilon}_{indi_s}\| \leq \varepsilon^\star$.

The difference equation of $\boldsymbol{\sigma}(k)$ is

$$\Delta\boldsymbol{\sigma}(k) = \boldsymbol{\sigma}(k+1) - \boldsymbol{\sigma}(k) = h\boldsymbol{SB}_c\left(\boldsymbol{\varepsilon}_{indi_s}(k) - \boldsymbol{K}_s sgn(\boldsymbol{\sigma}(k))^\gamma\right) \tag{32}$$

Then, every element in $\Delta\boldsymbol{\sigma}(k)$ is calculated by

$$\Delta\sigma_i(k) = h\varepsilon_{indi_s,i}(k) - hK_{s,i}|\sigma_i(k)|^\gamma sign(\sigma_i(k)) \tag{33}$$

- *When the sliding variable $\sigma_i(k) > 0$, this yields*

$$\Delta\sigma_i(k) = -hK_{s,i}|\sigma_i(k)|_i^\gamma + h\varepsilon_{indi_s,i}(k) \tag{34}$$

It is observed that $\forall\sigma_i(k) \geq \left(\frac{\varepsilon^\star}{K_{s,i}}\right)^{\frac{1}{\gamma_i}}, \Delta\sigma_i(k) < 0, \sigma_i(k)$ decreases, until it enters the range $0 < \sigma_i(k) \leq \left(\frac{\varepsilon^\star}{K_{s,i}}\right)^{\frac{1}{\gamma_i}}$.

- *When the sliding variable $\sigma_i(k) < 0$, Eq. (32) becomes*

$$\Delta\sigma_i(k) = hK_{s,i}|\sigma_i(k)|_i^\gamma + h\varepsilon_{indi_s,i}(k) \tag{35}$$

It is observed that $\forall\sigma_i(k) \leq -\left(\frac{\varepsilon^\star}{K_{s,i}}\right)^{\frac{1}{\gamma_i}}, \Delta\sigma_i(k) > 0, \sigma_i(k)$ increases, until it enters the range $\left(\frac{\varepsilon^\star}{K_{s,i}}\right)^{\frac{1}{\gamma_i}} < \sigma_i(k) < 0$.

Then the ultimate bound of $\sigma_i(k)$ equals $\bar{\delta}_{s,i} = \left(\frac{\varepsilon^\star}{K_{s,i}}\right)^{\frac{1}{\gamma_i}}$, whose size can be made arbitrarily small. Therefore, the control will lead to sliding motion in finite time T_1 such that $|\sigma_i(k)| < \bar{\delta}_{s,i}$.

Denote the sliding variable in a quasi-sliding motion as $\boldsymbol{\sigma}(k) = \tilde{\boldsymbol{d}}(k)$ and $\bar{\delta}_s = \sup_{i=1,\ldots,m}\left(\frac{\varepsilon^\star}{K_{s,i}}\right)^{\frac{1}{\gamma_i}}$, then $|\tilde{d}_i(k)| < \bar{\delta}_{s,i} \leq \bar{\delta}_s$. The quasi-sliding mode dynamics equation can be written by:

$$\boldsymbol{e}(k+1) = [\boldsymbol{I} + h(\boldsymbol{A}_c - \boldsymbol{B}_c\boldsymbol{K})]\boldsymbol{e}(k) + \boldsymbol{B}_c(\boldsymbol{SB}_c)^{-1}(\tilde{\boldsymbol{d}}(k+1) - \tilde{\boldsymbol{d}}(k)) \tag{36}$$

where $\tilde{\boldsymbol{d}}(k)$ has a magnitude of $O(\bar{\delta}_s)$ due to the non-ideal sliding motion. Recall that $\rho(\boldsymbol{I} + h(\boldsymbol{A}_c - \boldsymbol{B}_c\boldsymbol{K})) \leq \bar{\lambda} < 1$. Eq. (36) indicates that the tracking error will converge to a small bound related to $\bar{\delta}_s$. As a consequence, the following equation holds:

$$\|\boldsymbol{e}(k+1)\| \leq \bar{\lambda}^k\|\boldsymbol{e}(0)\| + \frac{h(1-\bar{\lambda}^k)}{1-\bar{\lambda}}2mc_0\bar{\delta}_s \tag{37}$$

where $c_0 = \|\boldsymbol{B}_c(\boldsymbol{SB}_c)^{-1}\|$. Using the fact $\bar{\lambda} < 1$, it follows that

$$\lim_{k\to\infty}\|\boldsymbol{e}(k+1)\| \leq \frac{2hmc_0\bar{\delta}_s}{1-\bar{\lambda}} \tag{38}$$

Since the reference signal $\boldsymbol{r}$ is designed to be bounded $\boldsymbol{r} \in \mathcal{L}_\infty$, it can be shown that $\boldsymbol{\xi} \in \mathcal{L}_\infty$.

7

Regarding the internal dynamics, choose $V_{in}(\boldsymbol{\eta})$ defined in $D_{\eta} = \{\boldsymbol{\eta} \in \mathbb{R}^{n-\rho}\}$ as the candidate Lyapunov function for $\dot{\boldsymbol{\eta}} = \boldsymbol{f}_{in}(\boldsymbol{\eta}, \boldsymbol{\xi})$. Since the origin $\dot{\boldsymbol{\eta}} = \boldsymbol{f}_{in}(\boldsymbol{\eta}, \boldsymbol{0})$ is globally exponentially stable, then there exists class $\mathcal{K}_{\infty}$ functions α'_1 and α'_2 such that $\alpha'_1(\|\boldsymbol{e}\|) \leq \|V_{in}(\boldsymbol{\eta})\| \leq \alpha'_2(\|\boldsymbol{e}\|)$ is satisfied. In the meanwhile, $V_{in}(\boldsymbol{\eta})$ satisfies $\frac{\partial V_{in}}{\partial \boldsymbol{\eta}} \boldsymbol{f}_{in}(\boldsymbol{\eta}, \boldsymbol{0}) \leq -c_3 \|\boldsymbol{\eta}\|^2$, $\|\frac{\partial V_{in}}{\partial \boldsymbol{\eta}}\| \leq c_4 \|\boldsymbol{\eta}\|$ for some positive constants c_3 and c_4. Due to the fact that $\boldsymbol{f}_{in}(\boldsymbol{\eta}, \boldsymbol{\xi})$ is continuously differentiable and globally Lipschitz in $(\boldsymbol{\eta}, \boldsymbol{\xi})$, then there exists a global Lipschitz constant L such that $\|\boldsymbol{f}_{in}(\boldsymbol{\eta}, \boldsymbol{\xi}) - \boldsymbol{f}_{in}(\boldsymbol{\eta}, \boldsymbol{0})\| \leq L(\|\boldsymbol{e}\| + \|\boldsymbol{r}\|), \forall \boldsymbol{\eta} \in \mathbb{R}^{n-\rho}$. As a result, the time derivative of $V_{in}(\boldsymbol{\eta})$ satisfies [9]

$$\dot{V}_{in}(\boldsymbol{\eta}) = \frac{\partial V_{in}}{\partial \boldsymbol{\eta}} \boldsymbol{f}_{in}(\boldsymbol{\eta}, \boldsymbol{\xi}) \leq -c_3 \|\boldsymbol{\eta}\|^2 + c_4 L \|\boldsymbol{\eta}\|(\|\boldsymbol{e}\| + \|\boldsymbol{r}\|) \leq -c_3(1 - \theta_1)\|\boldsymbol{\eta}\|^2, \quad \forall \|\boldsymbol{\eta}\| \geq \frac{c_4 L(\|\boldsymbol{e}\| + \|\boldsymbol{r}\|)}{c_3 \theta_1} \quad (39)$$

with constant $\theta_1 \in (0, 1)$. Denote the initial time point as t_0, and

$$\mu \triangleq \frac{c_4 L}{c_3 \theta_1} \left(\sup_{t_0 + T_1 \leq \tau \leq t} (\|\boldsymbol{e}\| + \|\boldsymbol{r}\|) \right) \quad (40)$$

As a result, there exists a class $\mathcal{KL}$ function β' such that

$$\|\boldsymbol{\eta}\| \leq \beta'(\|\boldsymbol{\eta}(t_0 + T_1)\|, t - t_0 - T_1) + \alpha_1'^{-1}(\alpha'_2(\mu)), \quad \forall t \geq t_0 + T_1 \quad (41)$$

Then the normal value of the internal state satisfies

$$\|\boldsymbol{\eta}\| \leq \theta_2 \varepsilon^{\star} + \alpha_1'^{-1} \left(\alpha'_2 \left(\frac{c_4 L}{c_3 \theta_1} \left(\frac{2hmc_0 \bar{\delta}_s}{1 - \bar{\lambda}} + \bar{r} \right) \right) \right), \quad \forall t \geq t_0 + T_1 + T_2 \quad (42)$$

for some finite $T_2 > 0$ and $\theta_2 > 0$, where $\bar{r}$ is the upper bound of $\|\boldsymbol{r}\|$. This shows that $\boldsymbol{\eta}$ is globally ultimately bounded by a class $\mathcal{K}$ function of $\bar{\lambda}, \bar{\delta}_s$, and $\bar{r}$.

This completes the proof.

Remark 3 *For the nonlinear system modelled in Eq. (19), the term $\boldsymbol{\Phi}_0(\boldsymbol{x})$ in Eq. (12) equals $\boldsymbol{I} - \bar{\mathcal{B}}_0(x)\boldsymbol{\Lambda}\bar{\mathcal{B}}_0^{-1}(x)$. It can be observed that if $-2 < w_i < 0$, then $\rho(\boldsymbol{\Phi}_0(\boldsymbol{x})) = \rho(\boldsymbol{I} - \boldsymbol{\Lambda}) > 1$. As a consequence, the boundedness of the perturbation term in Eq. (12), as well as the closed-loop stability of conventional INDI cannot be guaranteed. By contrast, the newly proposed discrete-time incremental sliding mode control has boarder applicability; because when $-2 < w_i < 0$, the condition $\rho(\boldsymbol{I} - |\boldsymbol{\Lambda}|) < 1$ still holds (Eq.(31)). Consequently, the stability of the closed-loop system is guaranteed.*

IV. Fault-tolerant Flight Control Design

In this section, an aircraft model with actuator faults and structural damage is described.

A. Equations of Motion

The nominal six degrees of freedom nonlinear equations of motion for a rigid aircraft in the body reference frame are given by

$$\begin{bmatrix} \dot{\boldsymbol{V}} \\ \dot{\boldsymbol{\omega}} \end{bmatrix} = \begin{bmatrix} -\tilde{\omega}\boldsymbol{V} + \frac{\boldsymbol{F}}{m_c} \\ -\boldsymbol{J}^{-1}\tilde{\omega}\boldsymbol{J}\boldsymbol{\omega} + \boldsymbol{J}^{-1}\boldsymbol{M} \end{bmatrix} \quad (43)$$

where $\boldsymbol{V} = [u, v, w]^{\mathsf{T}}$ and $\boldsymbol{\omega} = [p, q, r]^{\mathsf{T}}$ represent the translational and rotational velocities of the body-fixed frame with respect to the inertial frame, respectively. The inertia matrix is $\boldsymbol{J}$, which is defined as

$$\boldsymbol{J} = \begin{bmatrix} I_{xx} & 0 & -I_{xz} \\ 0 & I_{yy} & 0 \\ -I_{xz} & 0 & I_{zz} \end{bmatrix} \quad (44)$$

The operator $(\tilde{\cdot})$ denotes the skew-symmetric matrix of the corresponding vector $(\cdot)$. The $\boldsymbol{F}$ and $\boldsymbol{M}$ are the total external force and moment vectors, which incorporate gravitational, aerodynamic, and thrust forces and moments. A

typical model for the aerodynamic force $\boldsymbol{F}_a$ and moment $\boldsymbol{M}_a$ is in the following form:

$$\boldsymbol{M}_a = \bar{q}S\mathrm{diag}([b, \bar{c}, b])\left(\begin{bmatrix} C_l(\beta, r, p, Ma) \\ C_m(\alpha, q, Ma) \\ C_n(\beta, r, p, Ma) \end{bmatrix} + \begin{bmatrix} C_{l_{\delta_a}}(\alpha, \beta, Ma) & 0 & C_{l_{\delta_r}}(\alpha, \beta, Ma) \\ 0 & C_{m_{\delta_e}}(\alpha, Ma) & 0 \\ C_{n_{\delta_a}}(\alpha, \beta, Ma) & 0 & C_{n_{\delta_r}}(\alpha, \beta, Ma) \end{bmatrix}\begin{bmatrix} \delta_a \\ \delta_e \\ \delta_r \end{bmatrix}\right)$$

$$\boldsymbol{F}_a = \bar{q}S\left[C_x(\alpha, \beta, q, \delta_e, Ma), C_y(\alpha, \beta, p, r, \delta_a, \delta_r, Ma), C_z(\alpha, \beta, q, \delta_e, Ma)\right]^{\mathsf{T}} \tag{45}$$

where C_l, C_m, C_n are the rolling, pitching, and yawing moment coefficients, respectively. The dynamic pressure is $\bar{q} = 0.5\rho_a\|V\|_2^2$. The dynamics of β is derived as:

$$\dot{\beta} = \frac{1}{\sqrt{u^2 + w^2}}(F_{\beta,x} + F_{\beta,y} + F_{\beta,z}) + \frac{wp}{\sqrt{u^2 + w^2}} - \frac{ur}{\sqrt{u^2 + w^2}} \tag{46}$$

where

$$F_{\beta,x} = -\frac{uv}{V^2}(A_x - g\sin\theta), \quad F_{\beta,y} = (1 - \frac{v^2}{V^2})(A_y + g\sin\phi\cos\theta), \quad F_{\beta,z} = -\frac{vw}{V^2}(A_z + g\cos\phi\cos\theta) \tag{47}$$

and $\boldsymbol{A} = \frac{\boldsymbol{F}}{m_c} = [A_x, A_y, A_z]^{\mathsf{T}}$ denotes the specific force vector, g is the gravitational acceleration.

The kinematics for Euler angles $[\phi, \theta, \psi]^{\mathsf{T}}$ are given by

$$\begin{bmatrix} \dot{\phi} \\ \dot{\theta} \\ \dot{\psi} \end{bmatrix} = \begin{bmatrix} 1 & \sin\phi\tan\theta & -\cos\phi\tan\theta \\ 0 & \cos\phi & -\sin\phi \\ 0 & \sin\phi\sec\theta & \cos\phi\sec\theta \end{bmatrix}\begin{bmatrix} p \\ q \\ r \end{bmatrix} \tag{48}$$

1. Actuator Faults

Aircraft actuator faults include loss of control surface area, control surface jamming, and the oscillatory failure cases (OFCs). The inertial effects of actuator faults can be negligible. When an aircraft is subjected to the loss of control surface area fault, it leads to the loss of effectiveness for actuators, which can be modeled by

$$C'_{i_j} = \mu_j C_{i_j}, \quad \mu_j \in [0, 1], \quad i = l, m, n, \quad j = \delta_a, \delta_e, \delta_r \tag{49}$$

where $(\cdot')$ indicates the post-failure condition. Actuator jamming has two main impacts on system dynamics: 1) influence on control effectiveness; 2) induced extra forces and moments. If one side of the ailerons or elevators get stuck, the corresponding control derivatives are halved. Jamming faults also introduce new control derivatives such that the decoupling between longitudinal and lateral controls no longer holds. The aileron jamming would introduce $C_{m_{\delta_a}}$, and elevator jamming would introduce $C_{l_{\delta_e}}$ and $C_{n_{\delta_e}}$. If one of the ailerons is jammed at $\bar{\delta}_a$, the induced force and moment coefficients are

$$\Delta C_l = \frac{1}{2}C_{l_{\delta_a}}\bar{\delta}_a, \quad \Delta C_n = -\frac{1}{2}C_{n_{\delta_a}}\bar{\delta}_a, \quad \Delta C_y = \frac{1}{2}C_{y_{\delta_a}}\bar{\delta}_a, \quad \Delta C_z = \frac{C_{l_{\delta_a}}b}{r_{a_y}}, \quad \Delta C_m = -\frac{\Delta C_l b r_{a_x}}{\bar{c}r_{a_y}} \tag{50}$$

where where $\boldsymbol{r}_a = [r_{a_x}, r_{a_y}, r_{a_z}]^{\mathsf{T}}$ is the position vector from the center of mass (c.m.) to the aerodynamic center of the jammed aileron. The induced force and moment coefficients of one-side elevator jammed at $\bar{\delta}_e$ is calculated by

$$\Delta C_z = -\frac{C_{m_{\delta_e}}\bar{\delta}_e\bar{c}}{2r_{e_x}}, \quad \Delta C_m = \frac{1}{2}C_{m_{\delta_e}}\bar{\delta}_e, \quad \Delta C_l = \frac{\Delta C_z r_{e_y}}{b} \tag{51}$$

with $\boldsymbol{r}_e = [r_{e_x}, r_{e_y}, r_{e_z}]^{\mathsf{T}}$ indicates the position vector from the aircraft c.m. to the aerodynamic center of the jammed elevator.

The OFCs are mainly caused by electronic components in fault mode or by mechanical breakages. These malfunctions generate erroneous sinusoidal signals which propagate through the servo-loop control loop and may lead to unwanted control surface oscillations [20].

2. Structural Damage

Referring to the investigations in [17, 21], structural damage may lead to: the changes of aerodynamic properties, inertia properties, and the control effectiveness. In Ref. [21], the aircraft structural damage was modeled in the form of partial or complete tip loss of the horizontal stabilizers, the vertical tail, and the wings. Referring to the experiment results in [17, 21], it can be concluded that

- Structural damage changes the following mass and geometry properties of the aircraft: 1) total mass; 2) mean aerodynamic chords of lifting surfaces; 3) location of the center of mass; 4) moment of inertia.
- Structural damage also changes stability: 1) horizontal stabilizer damage varies the longitudinal stability; 2) vertical tail damage results in a change in lateral forces and directional stability; 3) wing damage reduces the lift force and causes unbalanced rolling moment.

Denote the distance vector from the original c.m. O to the new c.m. location O' as $\boldsymbol{r}_{OO'} = [r_{\Delta x}, r_{\Delta y}, r_{\Delta z}]^{\mathsf{T}}$. The equations of motion using the non-CM approach is given by [9, 10]

$$\begin{bmatrix} \dot{\boldsymbol{V}} \\ \dot{\boldsymbol{\omega}} \end{bmatrix} = \begin{bmatrix} m'\boldsymbol{I} & \tilde{\boldsymbol{S}}^{\mathsf{T}} \\ \tilde{\boldsymbol{S}} & \boldsymbol{J}' \end{bmatrix}^{-1} \begin{bmatrix} -m'\tilde{\boldsymbol{\omega}}\boldsymbol{V} - \tilde{\boldsymbol{\omega}}\tilde{\boldsymbol{S}}^{\mathsf{T}}\boldsymbol{\omega} + \boldsymbol{F}' \\ -\tilde{\boldsymbol{V}}\tilde{\boldsymbol{S}}^{\mathsf{T}}\boldsymbol{\omega} - \tilde{\boldsymbol{\omega}}\tilde{\boldsymbol{S}}\boldsymbol{V} - \tilde{\boldsymbol{\omega}}\boldsymbol{J}'\boldsymbol{\omega} + \boldsymbol{M}' \end{bmatrix} \tag{52}$$

where m' denotes the mass of the damaged aircraft; $\boldsymbol{J}'$ represents the inertia matrix of the damaged aircraft; $\boldsymbol{F}'$, $\boldsymbol{M}'$ denote the new total force and moment vectors after structural damage. $\boldsymbol{S} = [m'r_{\Delta x}, m'r_{\Delta y}, m'r_{\Delta z}]^{\mathsf{T}}$ is non-zero when using the non-CM approach, which leads to coupled translational and rotational motions. Using Eq. 52, the attitude dynamics of aircraft are

$$\dot{\boldsymbol{\omega}} = (\frac{1}{m'}\tilde{\boldsymbol{S}}\tilde{\boldsymbol{S}} + \boldsymbol{J}')^{-1}(\tilde{\boldsymbol{S}}\tilde{\boldsymbol{\omega}}\boldsymbol{V} - \frac{1}{m'}\tilde{\boldsymbol{S}}\tilde{\boldsymbol{\omega}}\tilde{\boldsymbol{S}}\boldsymbol{\omega} - \frac{1}{m'}\tilde{\boldsymbol{S}}\boldsymbol{F}' - \tilde{\boldsymbol{V}}\tilde{\boldsymbol{S}}^{\mathsf{T}}\boldsymbol{\omega} - \tilde{\boldsymbol{\omega}}\tilde{\boldsymbol{S}}\boldsymbol{V} - \tilde{\boldsymbol{\omega}}\boldsymbol{J}'\boldsymbol{\omega} + \boldsymbol{M}') \tag{53}$$

in which the translational and rotational dynamics are inertially coupled.

The influences of wing, horizontal stabilizer, and vertical tail damage on the aerodynamic coefficients of an aircraft are summarized in the Table. I of Ref. [10]. The changes in aerodynamic coefficients can be modeled by magnitude scaling [21]:

$$\begin{aligned} C'_x &= (1 + \Delta C_x) \cdot C_x, \quad C'_y = (1 + \Delta C_y) \cdot C_y, \quad C'_z = (1 + \Delta C_z) \cdot C_z \\ C'_m &= (1 + \Delta C_m) \cdot C_m, \quad C'_l = (1 + \Delta C_l) \cdot C_l, \quad C'_n = (1 + \Delta C_n) \cdot C_n \\ \Delta C_i &= \frac{C'_i - C_i}{|C_i|} \cdot 100\%, \quad i = x, y, z, m, l, n \end{aligned} \tag{54}$$

where C'_i, $i = x, y, z, m, l, n$ denote the post-damage aerodynamic coefficients.

B. Fault-tolerant Attitude Control Design

An attitude control system is designed to make the aircraft robustly track the roll and pitch angle references while minimizing the sideslip angle β. Consequently, the control variables are chosen as $\boldsymbol{y} = [\phi, \theta, \beta]^{\mathsf{T}}$. The nonlinear model corresponds to the motion of a rigid-body aircraft with $\boldsymbol{x}_1 = [\phi, \theta, \beta]^{\mathsf{T}}$, $\boldsymbol{x}_2 = [p, q, r]^{\mathsf{T}}$, $\boldsymbol{x} = [\boldsymbol{x}_1^{\mathsf{T}}, \boldsymbol{x}_2^{\mathsf{T}}]^{\mathsf{T}}$, and control input $\boldsymbol{u} = [\delta_a, \delta_e, \delta_r]^{\mathsf{T}}$ with the following representation:

$$\begin{cases} \dot{\boldsymbol{x}}_1 = \underbrace{\begin{bmatrix} 1 & \sin\phi\tan\theta & -\cos\phi\tan\theta \\ 0 & \cos\phi & -\sin\phi \\ \frac{w}{\sqrt{u^2+w^2}} & 0 & -\frac{u}{\sqrt{u^2+w^2}} \end{bmatrix}}_{\boldsymbol{g}_1(\boldsymbol{x}_1)} \boldsymbol{x}_2 + \underbrace{\begin{bmatrix} 0 \\ 0 \\ f_1(\boldsymbol{x}_1) \end{bmatrix}}_{\boldsymbol{f}_1(\boldsymbol{x}_1)} \\ \dot{\boldsymbol{x}}_2 = \underbrace{-\boldsymbol{J}^{-1}\tilde{\boldsymbol{\omega}}\boldsymbol{J}\boldsymbol{\omega} + \boldsymbol{J}^{-1}\boldsymbol{M}_f}_{\boldsymbol{f}_2(\boldsymbol{x})} + \underbrace{\boldsymbol{J}^{-1}\boldsymbol{C}_{M_u}}_{\boldsymbol{g}_2(\boldsymbol{x})} \boldsymbol{u} \\ \boldsymbol{y} = \boldsymbol{x}_1 \end{cases} \tag{55}$$

10

where

$$f_1(\boldsymbol{x}_1) = \frac{uvg\sin\theta + (V^2 - v^2)g\sin\phi\cos\theta - vwg\cos\phi\cos\theta}{V^2\sqrt{u^2 + w^2}} + \frac{-uvA_x + (V^2 - v^2)A_y - vwA_z}{V^2\sqrt{u^2 + w^2}}$$

$$\boldsymbol{C}_{M_u} = \bar{q}S\begin{bmatrix} bC_{l_{\delta_a}}(\alpha, \beta, Ma) & 0 & bC_{l_{\delta_r}}(\alpha, \beta, Ma) \\ 0 & \bar{c}C_{m_{\delta_e}}(\alpha, Ma) & 0 \\ bC_{n_{\delta_a}}(\alpha, \beta, Ma) & 0 & bC_{n_{\delta_r}}(\alpha, \beta, Ma) \end{bmatrix}, \quad \boldsymbol{M}_f = \bar{q}S\begin{bmatrix} bC_l(\beta, r, p, Ma) \\ \bar{c}C_m(\alpha, q, Ma) \\ bC_n(\beta, r, p, Ma) \end{bmatrix}$$

In Eq. (55), $\boldsymbol{V}, \alpha, \beta, A_x, A_y, A_z$ are measurable.

The aircraft dynamics considering model uncertainties, structure damage, and actuator faults are modeled as:

$$\begin{cases} \dot{\boldsymbol{x}}_1 = \boldsymbol{f}_1(\boldsymbol{x}_1) + \boldsymbol{g}_1(\boldsymbol{x}_1)\boldsymbol{x}_2 \\ \dot{\boldsymbol{x}}_2 = (1 - \kappa)\boldsymbol{f}_2(\boldsymbol{x}) + \kappa\boldsymbol{f}_2'(\boldsymbol{x}) + (1 - \kappa)\boldsymbol{g}_2(\boldsymbol{x})\boldsymbol{u} + \kappa\boldsymbol{g}_2'(\boldsymbol{x})\boldsymbol{u} \end{cases} \tag{56}$$

where $\kappa \in [0, 1]$ is designed as a unit step function to indicate sudden structure breaks and actuator faults during flight. In the new dynamics after sudden faults or damage, $\boldsymbol{f}_2'(\boldsymbol{x})$ and $\boldsymbol{g}_2'(\boldsymbol{x})$ are expressed as

$$\boldsymbol{f}_2'(\boldsymbol{x}) = (\frac{1}{m'}\tilde{\boldsymbol{S}}\tilde{\boldsymbol{S}} + \boldsymbol{J}')^{-1}(\tilde{\boldsymbol{S}}\tilde{\omega}\boldsymbol{V} - \frac{1}{m'}\tilde{\boldsymbol{S}}\tilde{\omega}\tilde{\boldsymbol{S}}\omega - \tilde{\boldsymbol{V}}\tilde{\boldsymbol{S}}^\top\omega - \tilde{\omega}\tilde{\boldsymbol{S}}\boldsymbol{V} - \tilde{\omega}\boldsymbol{J}'\omega - \frac{1}{m'}\tilde{\boldsymbol{S}}\boldsymbol{F}' + \boldsymbol{M}_f')$$

$$\boldsymbol{g}_2'(\boldsymbol{x}) = (\frac{1}{m'}\tilde{\boldsymbol{S}}\tilde{\boldsymbol{S}} + \boldsymbol{J}')^{-1}\boldsymbol{C}_{M_u}' = \boldsymbol{J}^{-1}\boldsymbol{C}_{M_u}\boldsymbol{\Lambda} + ((\frac{1}{m'}\tilde{\boldsymbol{S}}\tilde{\boldsymbol{S}} + \boldsymbol{J}')^{-1} - \boldsymbol{J}^{-1})\boldsymbol{C}_{M_u}\boldsymbol{\Lambda} \tag{57}$$

where the time varying diagonal matrix $\boldsymbol{\Lambda} \in \mathbb{R}^{3\times3}$ models the scaling of control effectiveness caused by damage and actuator faults. When $\kappa(t) = 0$, $\boldsymbol{\Lambda}(t)$ equals a three-by-three identity matrix.

The vector relative degree for $\boldsymbol{y} = [\phi, \theta, \beta]^\top$ is $\boldsymbol{\rho} = [2, 2, 2]^\top$. Therefore, the output dynamics of the aircraft attitude system are

$$\boldsymbol{y}^{(2)} = \frac{\partial[\boldsymbol{f}_1(\boldsymbol{x}_1) + \boldsymbol{g}_1(\boldsymbol{x}_1)\boldsymbol{x}_2]}{\partial\boldsymbol{x}_1}(\boldsymbol{f}_1(\boldsymbol{x}_1) + \boldsymbol{g}_1(\boldsymbol{x}_1)\boldsymbol{x}_2) + \boldsymbol{g}_1(\boldsymbol{x}_1)\left((1 - \kappa)\boldsymbol{f}_2(\boldsymbol{x}) + \kappa\boldsymbol{f}_2'(\boldsymbol{x}) + (1 - \kappa)\boldsymbol{g}_2(\boldsymbol{x})\boldsymbol{u} + \kappa\boldsymbol{g}_2'(\boldsymbol{x})\boldsymbol{u}\right) \tag{58}$$

which further leads to

$$\alpha(\boldsymbol{x}) = \frac{\partial[\boldsymbol{f}_1(\boldsymbol{x}_1) + \boldsymbol{g}_1(\boldsymbol{x}_1)\boldsymbol{x}_2]}{\partial\boldsymbol{x}_1}(\boldsymbol{f}_1(\boldsymbol{x}_1) + \boldsymbol{g}_1(\boldsymbol{x}_1)\boldsymbol{x}_2) + \boldsymbol{g}_1(\boldsymbol{x}_1)((1 - \kappa)\boldsymbol{f}_2(\boldsymbol{x}) + \kappa\boldsymbol{f}_2'(\boldsymbol{x})),$$

$$\mathcal{B}(\boldsymbol{x}) = \boldsymbol{g}_1(\boldsymbol{x}_1)\left((1 - \kappa)\boldsymbol{g}_2(\boldsymbol{x}) + \kappa\boldsymbol{g}_2'(\boldsymbol{x})\right) \tag{59}$$

Including the new variable κ in Eq. (56), the first-order Taylor series expansion of $\boldsymbol{y}^{(2)}$ is calculated by

$$\boldsymbol{y}^{(2)} = \boldsymbol{y}_0^{(2)} + \mathcal{A}_0(\boldsymbol{x}, \kappa)\Delta\boldsymbol{x} + \mathcal{B}_0(\boldsymbol{x}, \kappa)\Delta\boldsymbol{u} + \mathcal{H}_0(\boldsymbol{x}, \kappa)\Delta\kappa + \boldsymbol{R}_1(\boldsymbol{x}, \boldsymbol{u}, \kappa, h) \tag{60}$$

where $\mathcal{H}_0(\boldsymbol{x}) = \frac{\partial[\alpha(\boldsymbol{x}) + \mathcal{B}(\boldsymbol{x})\boldsymbol{u}]}{\partial\kappa}\Big|_0$. The discrete-time incremental sliding mode control in Eq. (22) is applied for the system Eq. (56) as

$$\Delta\boldsymbol{u}_{\text{indi-s}}(k) = \text{sgn}(\boldsymbol{\Lambda}(k))(\boldsymbol{g}_1(k)\boldsymbol{g}_2(k))^{-1}\left(\boldsymbol{v}_c(k) + \boldsymbol{v}_s(k) - \hat{\boldsymbol{y}}_0^{(2)}(k)\right) \tag{61}$$

Based on Eq. (60), the closed-loop system dynamics of Eq. (59) under the control input Eq. (61) are:

$$\boldsymbol{y}^{(2)}(k) = \boldsymbol{v}_c(k) + \boldsymbol{v}_s(k) + \underbrace{\tilde{\boldsymbol{\Delta}}_s(k) - \boldsymbol{\Phi}_s(k)(\boldsymbol{v}_c(k) + \boldsymbol{v}_s(k) - \boldsymbol{y}_0^{(2)}(k))}_{\varepsilon_{\text{indi}_s}(k)} \tag{62}$$

where $\boldsymbol{\Phi}_s(k)$ and $\tilde{\boldsymbol{\Delta}}_s(k)$ in Eq. (30) become

$$\boldsymbol{\Phi}_s(k) = \boldsymbol{I} - \boldsymbol{g}_1(k)\left((1 - \kappa(k))\boldsymbol{g}_2(k) + \kappa(k)\boldsymbol{g}_2'(k)\right)\text{sgn}(\boldsymbol{\Lambda}(k))(\boldsymbol{g}_1(k)\boldsymbol{g}_2(k))^{-1}$$

$$\tilde{\boldsymbol{\Delta}}_s(k) = \mathcal{A}_0(\boldsymbol{x}, \kappa)\Delta\boldsymbol{x} + \mathcal{H}_0(\boldsymbol{x}, \kappa)\Delta\kappa + \boldsymbol{R}_1(\boldsymbol{x}, \boldsymbol{u}, \kappa, h)\Big|_{\boldsymbol{x}=\boldsymbol{x}_0(k), \kappa=\kappa_0(k), \boldsymbol{u}=\boldsymbol{u}_0(k)+\Delta\boldsymbol{u}_{\text{indi-s}}(k)} + (\boldsymbol{I} - \boldsymbol{\Phi}_s(k))\tilde{\boldsymbol{y}}_0^{(2)}(k) \tag{63}$$

For an aircraft with actuator fault and structural damage, it is reasonable to assume that $\delta(k)$ is bounded [10]. Therefore, using Theorem 1, for faults and damage that satisfy $\rho(\boldsymbol{\Phi}_s(k)) < 1$, the post-fault aircraft can still track the given attitude commands.

11

V. Numerical Simulations

In this section, the discrete-time stability of INDI presented in Sec. II and the controller proposed in Sec. III will be numerically evaluated on a public model of F-16 [22]. Actuators are modelled as second-order linear systems with rate and position limits (parameters from the Table II of Ref. [10]). This aircraft is initially trimmed at a steady-level flight condition with airspeed $V = 600$ ft/s and altitude $h = 12,000$ ft. The initial states for the aircraft are $\boldsymbol{x}_1 = [0, 0, 0]^\circ, \boldsymbol{x}_2 = [0, 0, 0]^\circ/\text{s}$. The maximum magnitude of the random parametric uncertainties are chosen as

$$\Delta m_c = 5\%, \ \Delta S = 5\%, \ \Delta \bar{c} = 5\%, \ \Delta b = 5\%, \ \Delta I_{xx} = 10\%, \Delta I_{xz} = 10\%, \ \Delta I_{yy} = 10\%, \ \Delta I_{zz} = 20\%$$

The angular acceleration sensor is modeled with first-order linear system $G_a(s) = \frac{1}{0.033s+1}$. In addition, the height of the power spectral density (PSD) of the measurement noise of angular acceleration measurements are set to $1.0e^{-5}$.

For all the numerical simulations presented in this section, the control parameters are kept invariant for robustness testing as presented in Table 1.

Table 1 Control gains

Channel	INDI parameters		SMC parameters	
	$K_{i,0}$ in Eq. (22)	$K_{i,1}$ in Eq. (22)	$K_{s,i}$ in Eq. (27)	γ_i in Eq. (27)
Roll, ϕ	15	5	1	0.3
Pitch, θ	15	5	1	0.3
Sideslip, β	15	5	1	0.3

The fault cases considered in this section include the effectiveness loss of rudder, aileron, elevator, as well as structural damage. The influences of actuator faults and structural damage are modeled using the methods presented in Sec. IV. In simulations, two types of reference commands are designed: Type 1 is a smoothly filtered step; Type 2 is a single that smoothly combined from sigmoid functions. The simulated fault scenarios are as follows:

Scenario 1   Actuator faults, structural damage, and model uncertainties lead to $\|\boldsymbol{\Phi}_0(x)\| < 1$. To be specific, the aileron lost 50% of its effectiveness at 3 s with $w_1 = 0.5$, the elevator lost 30% of its effectiveness at 5 s with $w_2 = 0.7$, and the rudder has lost its effectiveness at 7 s with $w_3 = 0.6$. Moreover, the right aileron runs away and get jammed at $t = 3$ s with $\bar{\delta}_{a_r} = 15.05^\circ$. Also, at $t = 5$ s, the left elevator is jammed upwards at $\bar{\delta}_{e_l} = -12.5^\circ$. Apart from these actuator faults, the right wing lost 25% of its area at $t = 3$ s, the entire left horizontal stabilator is lost at $t = 5$ s, and a half of the vertical tail is lost at $t = 7$ s.

Scenario 2   Actuator faults, structural damage, and model uncertainties lead to $\|\boldsymbol{\Phi}_0(x)\| > 1$ in a short time period. This scenario is more severe than Scenario 1 as the aileron lost 70% of its effectiveness at $t = 3$ s, the elevator lost 50% of its the effectiveness at 5 s, and the left elevator is jammed upwards at $\bar{\delta}_{a_r} = -12.5^\circ$, while the rudder suddenly lost 60% of its effectiveness at $t = 7$ s, and the right aileron runs away and get jammed at $t = 3$ s with $\bar{\delta}_{a_r} = 15.05^\circ$. Apart from these, the structural damage situations are the same as those in scenario 1.

Scenario 3   Actuator faults, structural damage, model uncertainties and control reversal. In this case, the aileron lost 30% of its effectiveness at 3 s with $w_1 = 0.7$, and the rudder has lost its effectiveness at 7 s with $w_3 = 0.6$. The elevator lost 50% of its effectiveness at 5 s and changed its actuation sign periodically after $t = 7$s. Besides, the solid OFC fault is added to the left elevator from $t = 5$ s; the right wing lost 25% of its area at $t = 3$ s; and a half of the vertical tail is lost at $t = 10$ s.

In order to analyze the impacts of various sources of the uncertainty on the ultimate bound of the tracking errors, the trajectories of $\bar{\delta}_y(k) = \|\tilde{\boldsymbol{y}}_0(k)\|$, $\bar{\delta}_z(k) = \|\boldsymbol{y}^{(2)}(k) - \hat{\boldsymbol{y}}_0^{(2)}(k) - \boldsymbol{\mathcal{B}}_0(k)\Delta\boldsymbol{u}(k)\|$, and $\bar{\delta}_{v_c}(k) = \|\boldsymbol{v}_c(k) - \boldsymbol{v}_c(k-1)\|$ are plotted. Using Eq. (13) and Eq. (14), the estimated upper bound of the residual cancellation error of INDI-SMC is calculated by $\hat{\bar{\boldsymbol{\varepsilon}}}_{\text{indi}}(k) = \bar{b}^{k-k_0}\|\boldsymbol{\varepsilon}_{\text{indi}}(k_0)\| + \bar{b}\bar{\delta}_{v_c}(k-1) + (1-\bar{b})\bar{\delta}_y(k-1) + \bar{\delta}_z(k-1)$ in the simulation. Two performance metrics are used to evaluate the control performance. One is the root mean square (RMS) value of the tracking error. The other one is the integral of control cost (IAU): IAU $= \sum_{i=1}^3 \int_0^{t_f} |u_i(t)|dt$.

Table 2 shows the RMS value of the tracking error, IAU, and the maximum steady-state error in different simulation cases. As can be seen from Table 2 that the inclusion of sensing error (i.e., $\tilde{\boldsymbol{y}}^{(2)} \neq 0$) increases the maximum tracking error and the IAU. Nevertheless, the RMS values of the tracking errors are still comparable to the cases when $\tilde{\boldsymbol{y}}^{(2)} = 0$. This indicates that the INDI-SMC method has certain robustness against sensing error. As presented in the preceding

12

text, Scenario 2 is more severe than Scenario 1. Correspondingly, the RMS and maximum values of the tracking errors, as well as the IAU value are all higher in Scenario 2. Furthermore, because the control effectiveness of elevator changes its sign in Scenario 3, which violates the safety boundary of INDI-SMC, the closed-loop system becomes unstable. By contrast, the newly proposed D-INDI-SMC has boarder applicability, as the closed-loop system can tolerate the faults in Scenario 3 with reasonable tracking errors and control effort.

Table 2   Statistics for command tracking performance.

Scenario		1	1	2	2	3	3
Method		INDI-SMC	INDI-SMC	INDI-SMC	INDI-SMC	INDI-SMC	D-INDI-SMC
	$\tilde{\boldsymbol{y}}^{(2)}$	$\tilde{\boldsymbol{y}}^{(2)} = 0$	$\tilde{\boldsymbol{y}}^{(2)} \neq 0$	$\tilde{\boldsymbol{y}}^{(2)} = 0$	$\tilde{\boldsymbol{y}}^{(2)} \neq 0$	$\tilde{\boldsymbol{y}}^{(2)} \neq 0$	$\tilde{\boldsymbol{y}}^{(2)} \neq 0$
	$\boldsymbol{y}_r$	Type1	Type 1	Type 2	Type 2	Type 2	Type 2
RMS	ϕ	0.7904	0.7686	1.6592	1.5506	∞	0.2852
	θ	0.2370	0.2209	0.016	0.0142	∞	0.2934
	β	8.08e-04	0.001	0.0066	0.0068	∞	0.0019
IAU		124.2463	125.1224	323.6775	324.9343	–	230.9250
$\max(e_i)$	ϕ	0.00075	0.0048	0.0475	0.0728	∞	0.3496
	θ	0.00054	0.0025	0.0358	0.0447	∞	0.5345
	β	0.0032	0.0035	0.0358	0.0383	∞	0.0018

Scenario 1: Robustness to sensing error, actuator faults, and structural damage ($\|\boldsymbol{\Phi}_0(x)\| < 1$)   The results for the first scenario are illustrated in Fig. 1 - Fig. 4. The attitude tracking responses are given in Fig. 1. It can be observed that the bounded sensing error can be tolerated by the INDI control method. The sensing error can be seen in Fig. 2. When the sensing errors are included, larger control efforts are required, which can be seen from Fig. 3a and Table. 2. The responses of the sliding variables (Eq. (23)) are shown in Fig. 3b, in which all the variables converge into small bounds.

Figure 2 shows that the considered sensing errors result in a larger residual cancellation error of INDI-SMC as compared to the ideal case (with perfect estimate of $\boldsymbol{y}_0^{(2)}$). The first and third subplots of Fig. 4 show that the variations of $\bar{\delta}_y$, $\bar{\delta}_z$, and $\bar{\delta}_{v_c}$ are mainly induced by the command variations, faults, and damage in the system. Comparing the relative magnitudes of the uncertainties, the third subplot of Fig. 4 shows that $\bar{\delta}_z$ has the highest magnitude throughout the time history, which is followed by $\bar{\delta}_y$. As explained in Sec. II, under high sampling frequency, the variations of virtual control has limited impacts on the closed-loop behaviour, which is verified by the small magnitude of $\bar{\delta}_{v_c}$. After faults occur, all the three uncertainty terms gradually converge to a small bound around zero. The forth subplot of Fig. 4 verifies that the real $\|\boldsymbol{\varepsilon}_{\text{indi}}\|$ is indeed always smaller than its estimated bound given in Eq. (14). Furthermore, $\|\boldsymbol{\varepsilon}_{\text{indi}}(k)\|$ is ultimately bounded which verifies Eq. (15).
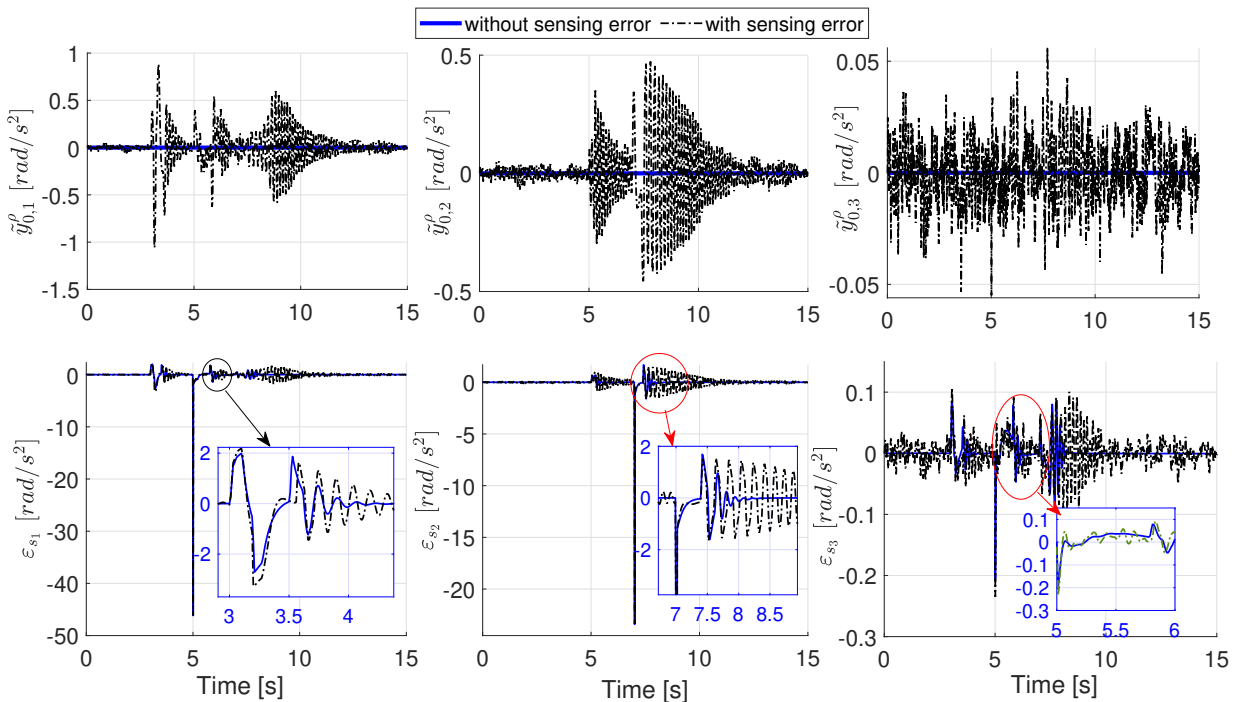
Scenario 2: Robustness to sensing error as well as severe faults and damage ($\|\boldsymbol{\Phi}_0(x)\| > 1$ **in short time intervals)** The simulation results are showed in Fig. 5 - Fig. 8. Even through $\|\boldsymbol{\Phi}_0(x)\| > 1$ happens in short time intervals $t \in [3, 3.96]$ s and $[5.35, 7]$ s (Fig. 8), the tracking performance is still acceptable (Fig. 5 and Table 2). According to the investigation in [23], a system under FTC is stable if the activating period of stable modes is long enough compared with that of the unstable mode. It can be seen from Fig. 6, although $\|\boldsymbol{\Phi}_0(x)\| > 1$ occurs, the residual cancellation error $\boldsymbol{\varepsilon}_{\text{INDI}}$ remains bounded. This leads to a conclusion that the INDI-SMC control still has some robustness even in the transient period where the estimation error of $\mathcal{B}_0(\boldsymbol{x})$ exceeds the uncertain limits and shortly violates the restriction of $\|\boldsymbol{\Phi}_0(x)\| < 1$.

As compared to the Scenario 1, both the tracking tasks and fault cases in Scenario 2 are more challenging. Even so, Fig. 6 shows the residual cancellation error of INDI-SMC remain bounded. Also, Fig. 7b shows that the sliding mode variables are also bounded. In view of Fig. 6 and Fig. 8, the spikes of $\bar{\delta}_i$ and $\boldsymbol{\varepsilon}_{\text{INDI}}$ are mainly caused by reference command variations and fault injections.

13
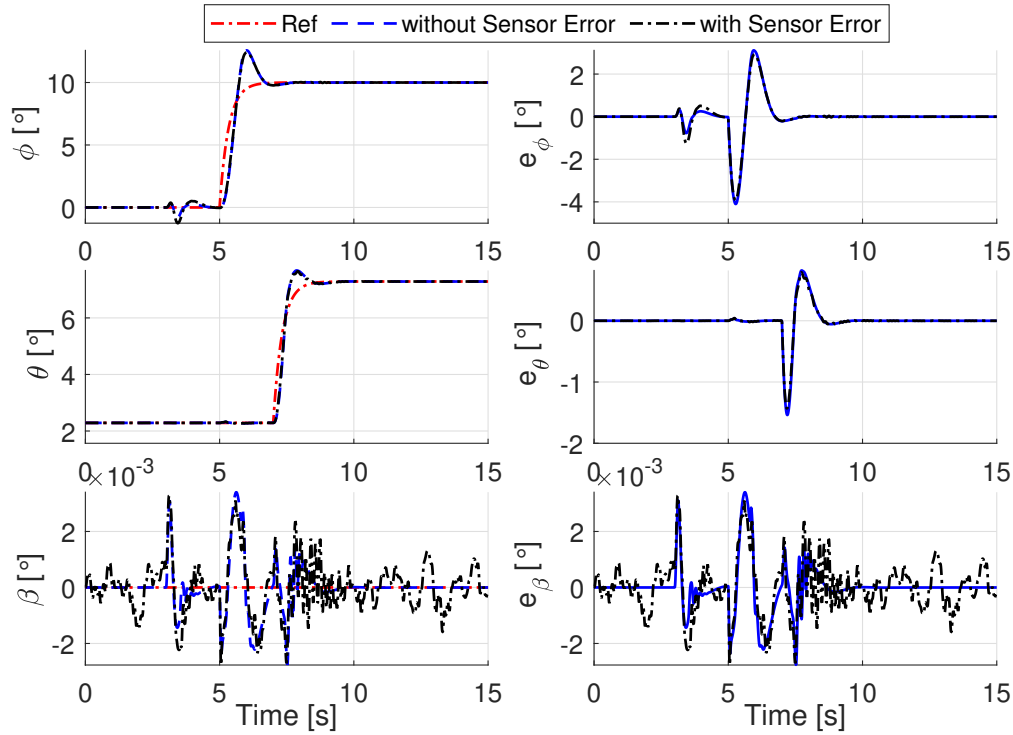
Fig. 1   Scenario 1: attitude tracking performance of INDI-SMC.


Fig. 2   Scenario 1: sensing error and the residual cancellation error of INDI-SMC.

Scenario 3: Robustness to sensing error and control reversal   The aircraft responses in Scenario 3 are shown in Figs. 9-12. Figure 9 shows that INDI-SMC is unstable to stabilize the aircraft with sensing error and control reversal
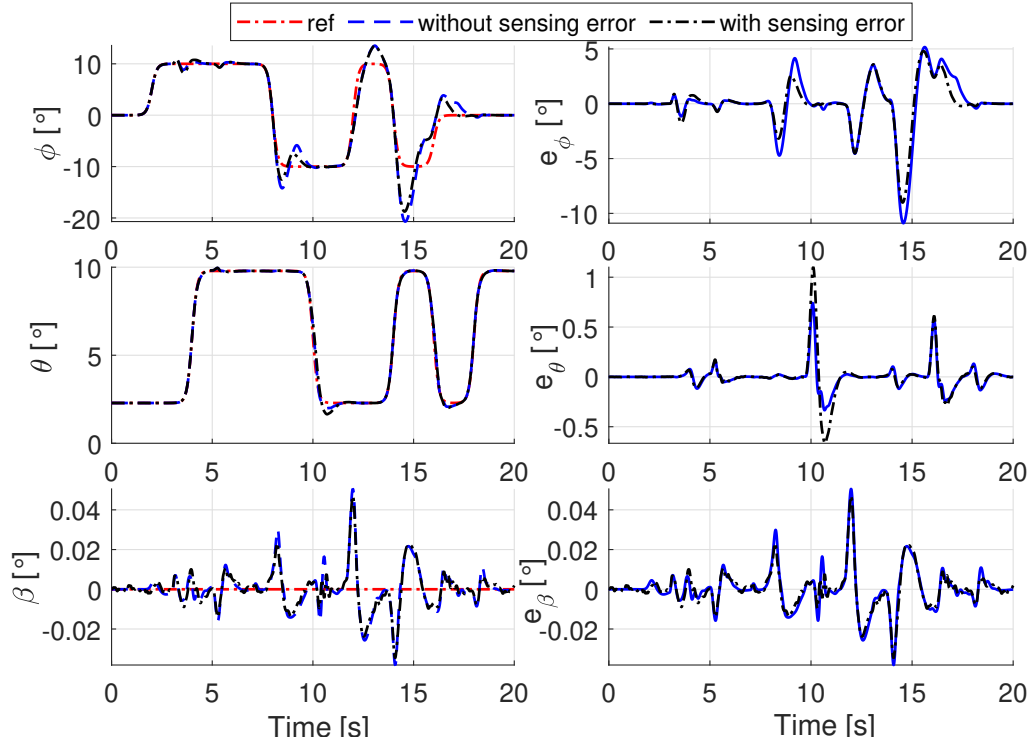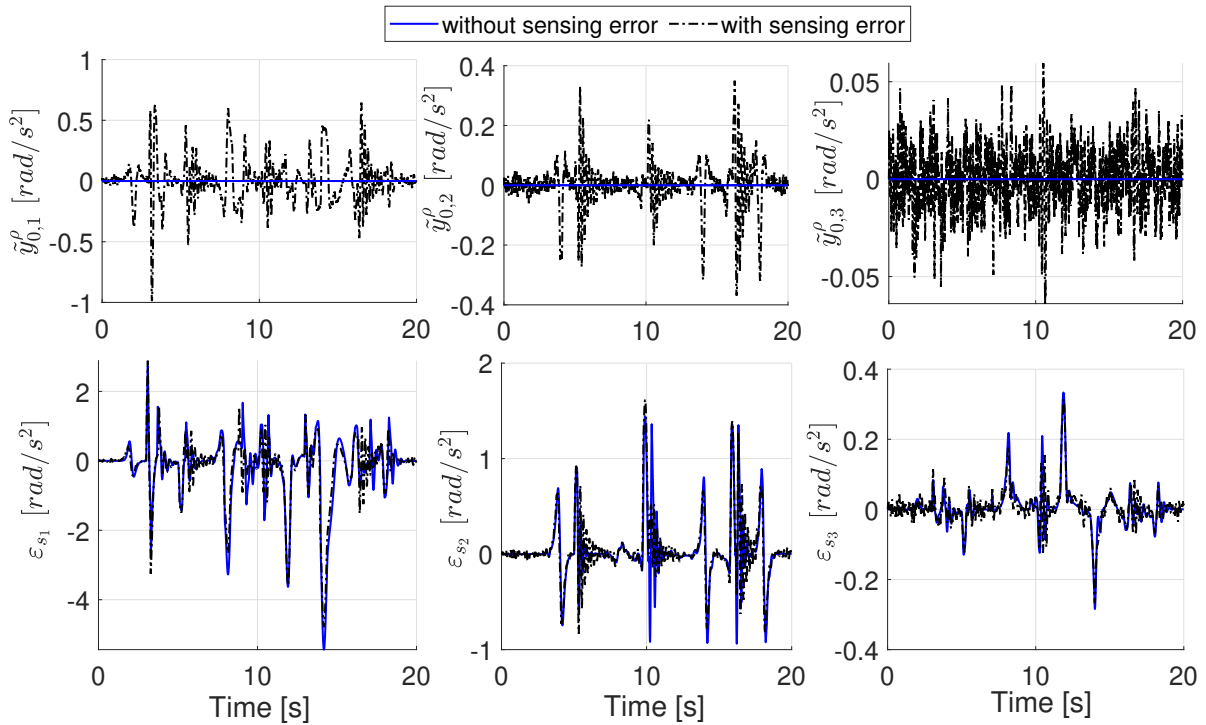
14

(a) Control inputs

(b) Sliding mode variables
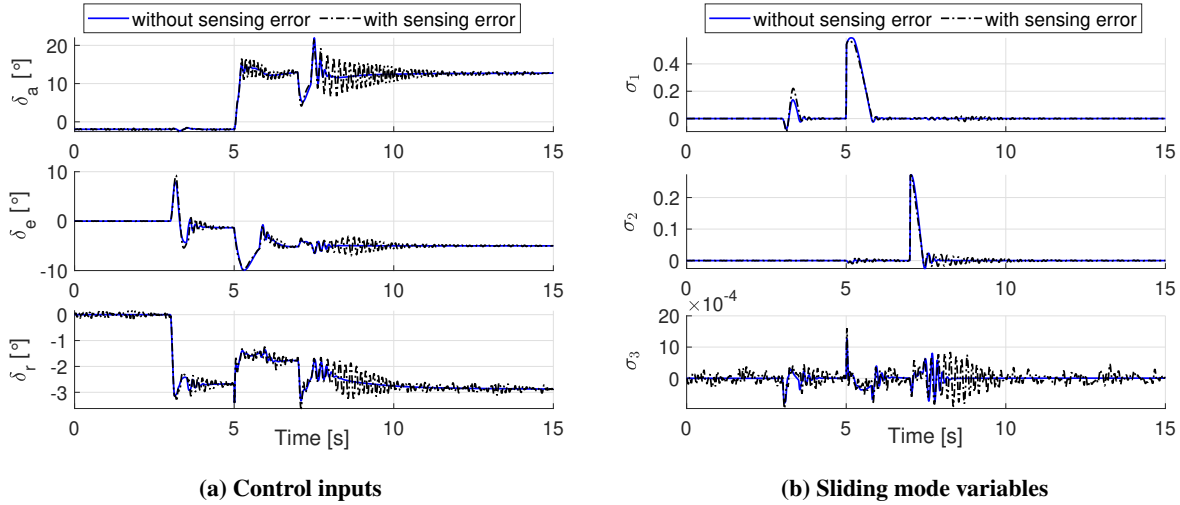
Fig. 3   Scenario 1: control inputs and sliding mode variable responses.
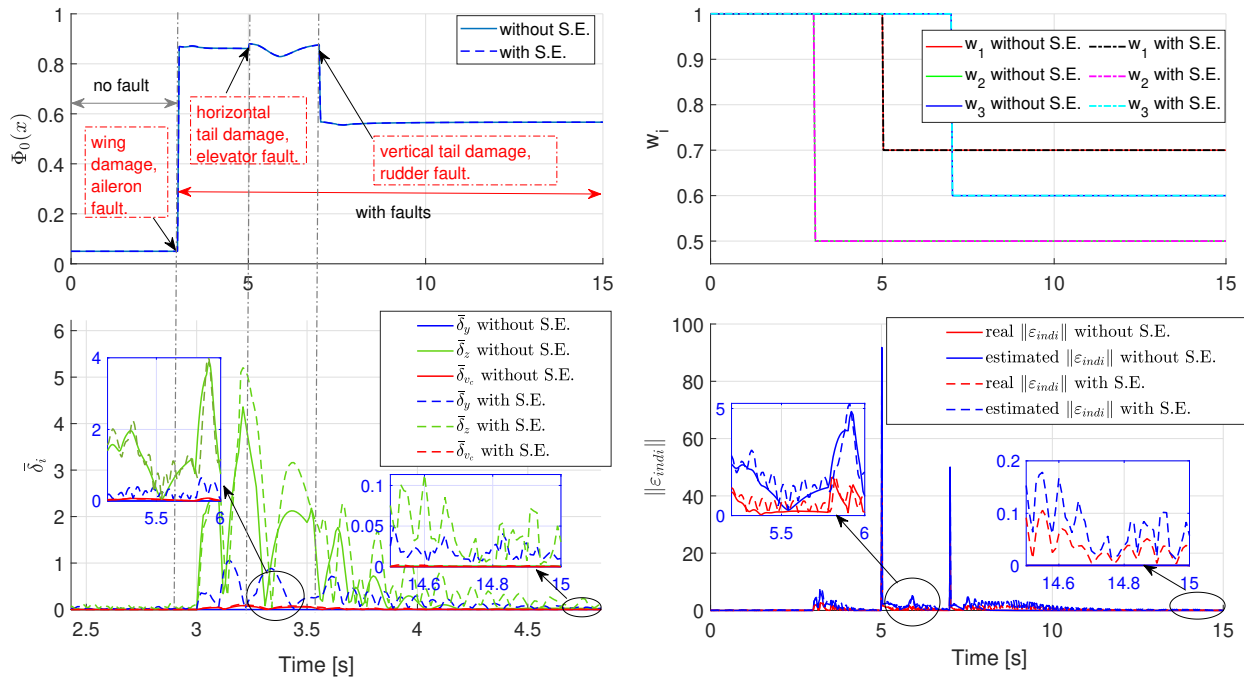
Fig. 4   Scenario 1 : responses of $\Phi_0(x)$ and the bounds of uncertainties (S.E. represents sensing error).

while the newly proposed D-INDI-SMC is able to tolerate the faults and execute the tracking commands. The control reversal happens in every 5 s during simulation, which can be seen from the second subplot of Fig. 12. It can be observed from Fig. 10 that INDI-SMC presents loss of control since control reversal breaks its stable condition $\|\Phi_0(x)\| < 1$ (show in Fig. 12); its resulting residual error and sliding variables (Fig. 11b) also become unbounded. By contrast, D-INDI-SMC does not presents actuator saturation (Fig. 10); its tracking performance is also comparable to that in Scenario 1 (see Table. 2). Furthermore, the residual cancellation error and sliding variables using D-INDI-SMC remain bounded as shown in Fig. 10 and Fig. 11b. The simulation results of Scenario 3 conclude that the D-INDI-SMC method proposed in this paper has higher robustness against control reversal as compared to INDI-SMC in the literature.
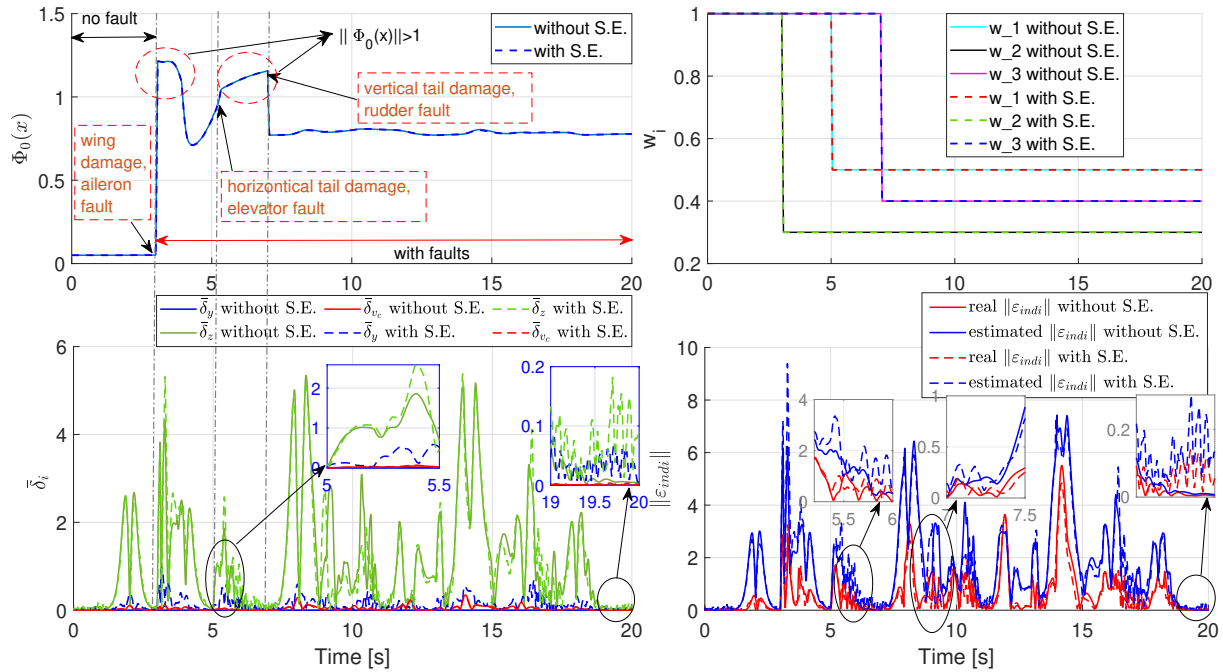
15

Fig. 5 Scenario 2: attitude tracking performance of INDI-SMC.

Fig. 6 Scenario 2: sensing error and the residual cancellation error of INDI-SMC.
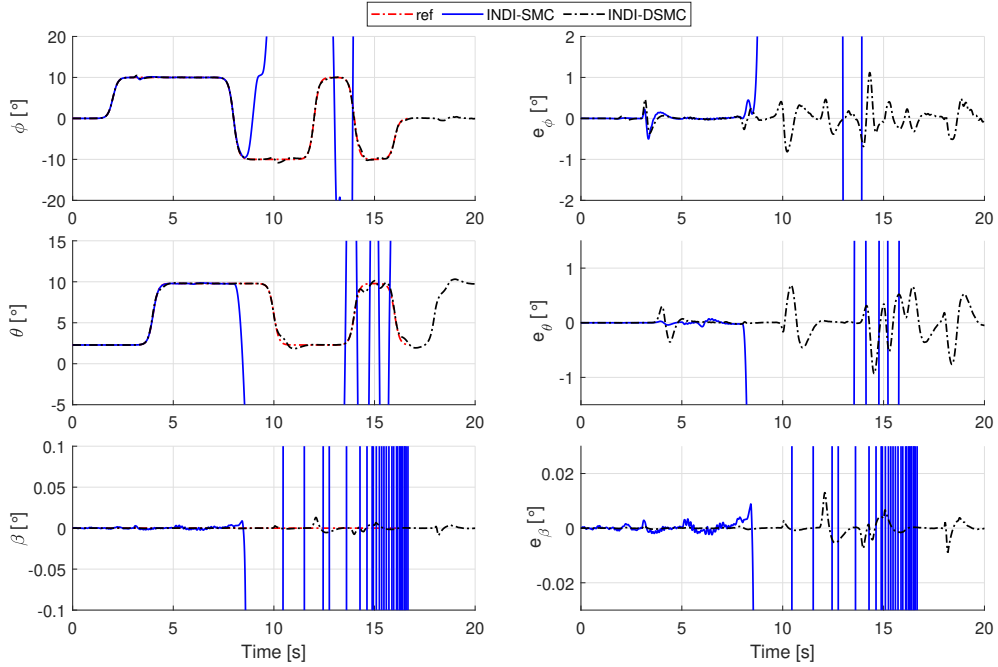
(a) Control inputs

(b) sliding mode variables
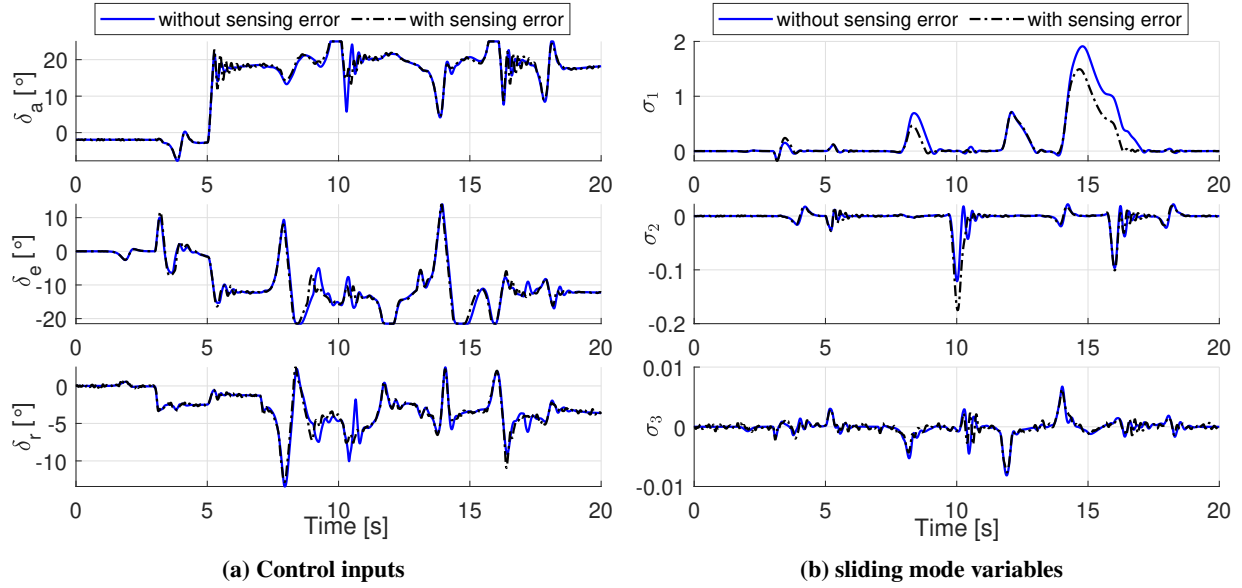
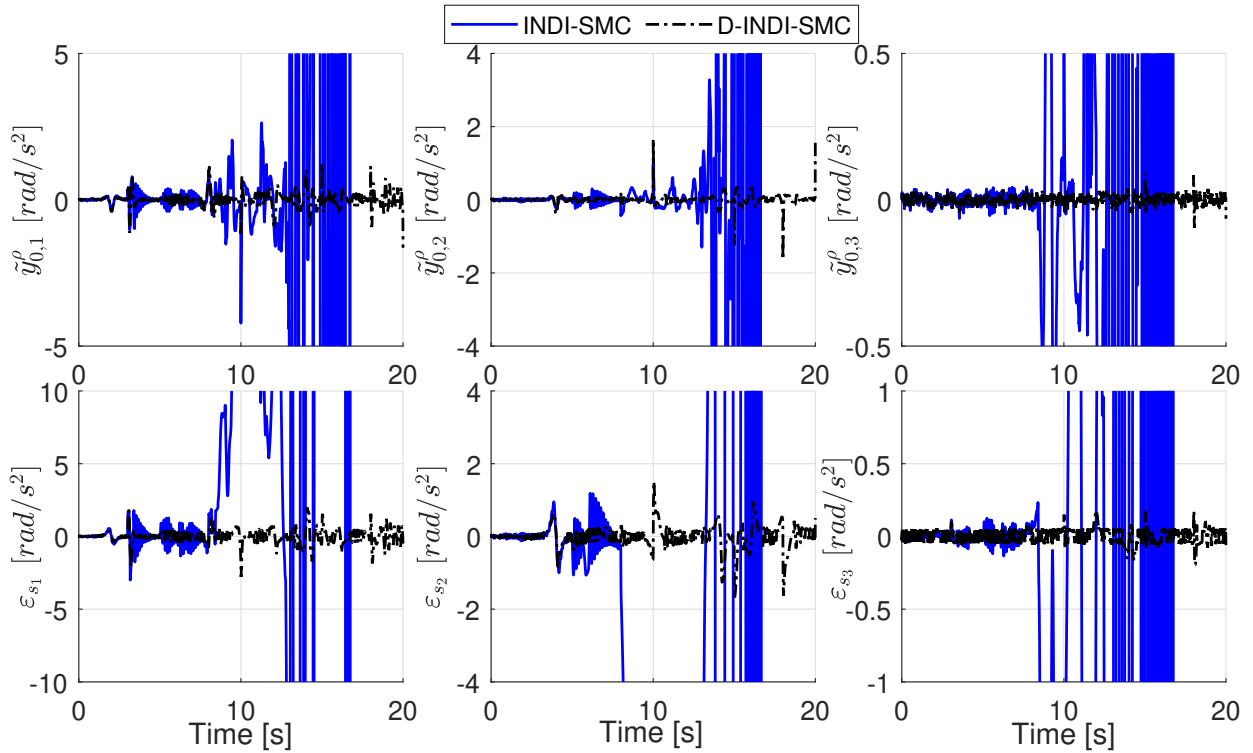**Fig. 7   Scenario 2: control inputs and sliding mode variable responses.**

Fig. 8   Scenario 2 : responses of $\Phi_0(x)$ and the bounds of uncertainties (S.E. represents sensing error).

VI. Conclusions

By virtue of its sensor-based structure, the incremental control shows promising robustness against aircraft model uncertainties, sudden actuator faults, and structural damage. This paper has shown that the performance of INDI is influenced by sensing errors and control effectiveness estimation errors. It has been proved that the sensitivity of INDI to sensing error, incremental dynamic approximation error, faults, and damage decreases as the sampling frequency increases. Numerical simulations show that critical loss of actuator effectiveness can result in significant performance

Fig. 9   Scenario 3: attitude tracking performance of INDI-SMC and D-INDI-SMC.


Fig. 10   Scenario 3: sensing error and the residual error of INDI-SMC and D-INDI-SMC.

degradation and even loss of control. One special severe actuator fault case is the control reversal, which leads to the instability of the incremental sliding mode control (INDI-SMC) method in the literature. In view of this, this paper proposes a discrete-time control direction-based incremental sliding mode control, denoted as D-INDI-SMC with

(a) Control inputs　　　　　　　　**(b) sliding mode variables**
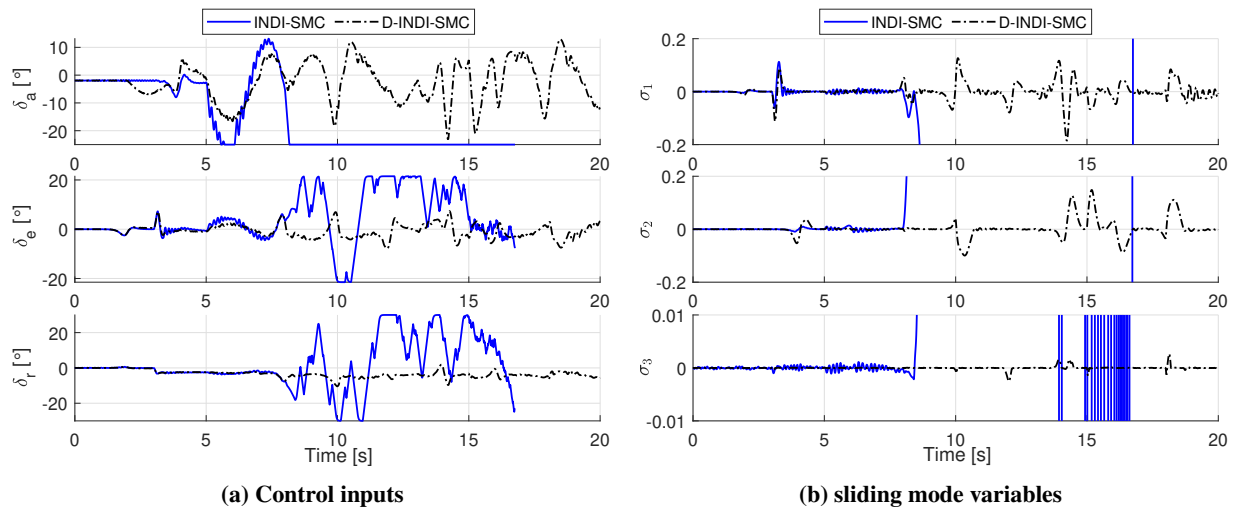
Fig. 11　Scenario 3: control inputs and sliding mode variable responses.
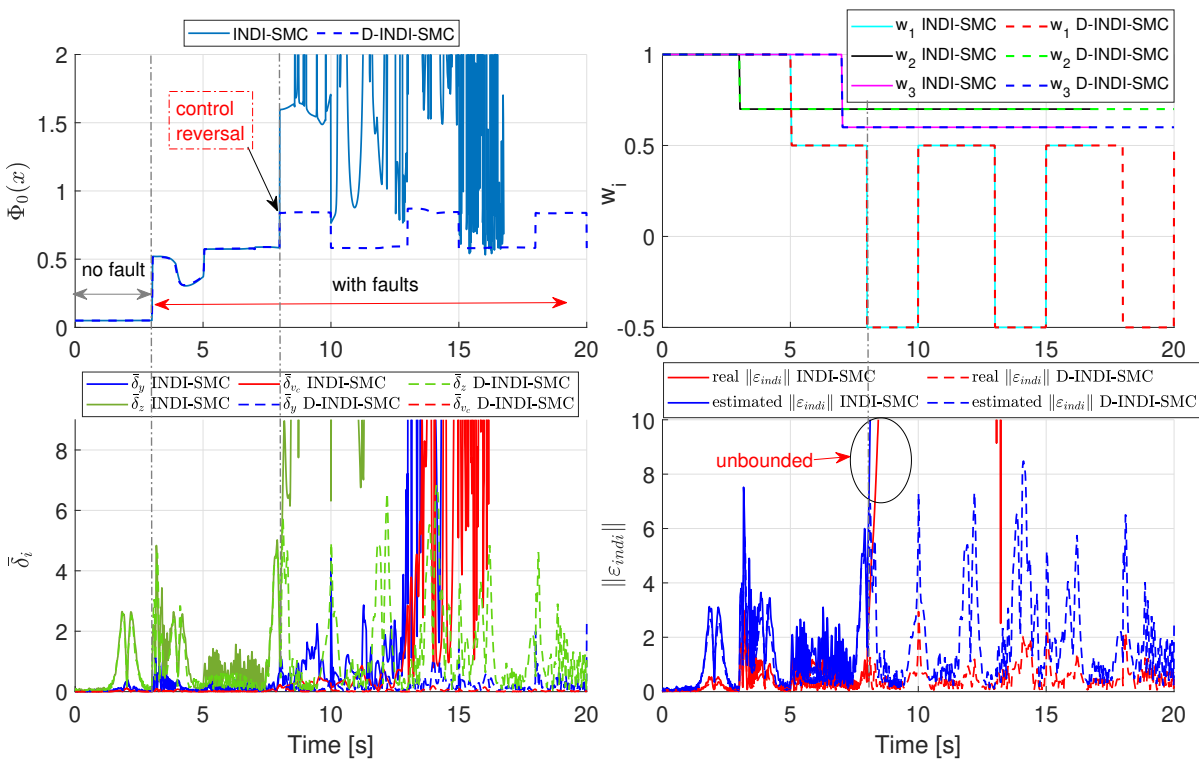
Fig. 12　Scenario 3: responses of $\Phi_0(x)$ and the bounds of uncertainties.

guaranteed stability in the Lyapunov sense. The effectiveness of this method is verified by simulations on an attitude tracking problem of an aircraft subjects to control reversal, sensing errors, actuator faults, and structural damage. Future work will seek the possibility to relax the assumptions and stability criteria in the proposed method.

References

[1] Zolghadri, A., "On flight operational issues management: Past, present and future," *Annual Reviews in Control*, Vol. 45, 2018, pp. 41–51. https://doi.org/10.1016/j.arcontrol.2018.03.001.

19

[2] Bošković, J. D., and Mehra, R. K., "Failure detection, identification and reconfiguration in flight control," *Fault Diagnosis and Fault Tolerance for Mechatronic Systems: Recent Advances*, Springer Berlin Heidelberg, 2003, pp. 129–167. https://doi.org/10.1007/3-540-45737-2_5.

[3] Zolghadri, A., Henry, D., Cieslak, J., Efimov, D., and Goupil, P., *Fault diagnosis and fault-tolerant control and guidance for aerospace vehicles*, Springer London, 2014. https://doi.org/10.1007/978-1-4471-5313-9.

[4] Sieberling, S., Chu, Q., and Mulder, J., "Robust flight control using incremental nonlinear dynamic inversion and angular acceleration prediction," *Journal of guidance, control, and dynamics*, Vol. 33, No. 6, 2010, pp. 1732–1742. https://doi.org/10.2514/1.49978.

[5] van Ekeren, W., Looye, G., Kuchar, R. O., Chu, Q. P., and van Kampen, E.-J., "Design, Implementation and Flight-Tests of Incremental Nonlinear Flight Control Methods," American Institute of Aeronautics and Astronautics, 2018, p. 384. https://doi.org/10.2514/6.2018-0384.

[6] Smeur, E. J., Chu, Q., and de Croon, G. C., "Adaptive incremental nonlinear dynamic inversion for attitude control of micro air vehicles," *Journal of Guidance, Control, and Dynamics*, Vol. 39, No. 3, 2016, pp. 450–461. https://doi.org/10.2514/1.G001490.

[7] Jeon, B.-J., Seo, M.-G., Shin, H.-S., and Tsourdos, A., "Understandings of classical and incremental backstepping controllers with model uncertainties," *IEEE Transactions on Aerospace and Electronic Systems*, Vol. 56, No. 4, 2019, pp. 2628–2641. https://doi.org/10.1109/TAES.2019.2952631.

[8] Jeon, B.-J., Seo, M.-G., Shin, H.-S., and Tsourdos, A., "Understandings of incremental backstepping controller considering measurement delay with model uncertainty," *Aerospace Science and Technology*, Vol. 109, 2021, p. 106408. https://doi.org/10.1016/j.ast.2020.106408.

[9] Wang, X., Van Kampen, E.-J., Chu, Q., and Lu, P., "Stability analysis for incremental nonlinear dynamic inversion control," *Journal of Guidance, Control, and Dynamics*, Vol. 42, No. 5, 2019, pp. 1116–1129. https://doi.org/10.2514/1.G003791.

[10] Wang, X., van Kampen, E.-J., Chu, Q., and Lu, P., "Incremental sliding-mode fault-tolerant flight control," *Journal of guidance, control, and dynamics*, Vol. 42, No. 2, 2019, pp. 244–259. https://doi.org/10.2514/1.G003497.

[11] Wang, X., Sun, S., van Kampen, E.-J., and Chu, Q., "Quadrotor fault tolerant incremental sliding mode control driven by sliding mode disturbance observers," *Aerospace Science and Technology*, Vol. 87, 2019, pp. 417–430. https://doi.org/10.1016/j.ast.2019.03.001.

[12] van Gils, P., van Kampen, E.-J., de Visser, C. C., and Chu, Q. P., "Adaptive incremental backstepping flight control for a high-performance aircraft with uncertainties," *AIAA Guidance, Navigation, and Control Conference*, 2016, p. 1380. https://doi.org/10.2514/6.2016-1380.

[13] Bhardwaj, P., Akkinapalli, V. S., Zhang, J., Saboo, S., and Holzapfel, F., "Adaptive augmentation of incremental nonlinear dynamic inversion controller for an extended f-16 model," *AIAA Scitech 2019 Forum*, 2019, p. 1923. https://doi.org/10.2514/6.2019-1923.

[14] Guo, Z., Guo, J., Zhou, J., and Chang, J., "Robust tracking for hypersonic reentry vehicles via disturbance estimation-triggered control," *IEEE Transactions on Aerospace and Electronic Systems*, Vol. 56, No. 2, 2019, pp. 1279–1289. https://doi.org/10.1109/TAES.2019.2928605.

[15] Ma, Y., Ren, H., Tao, G., and Jiang, B., "Adaptive Compensation for Actuation Sign Faults of Flexible Spacecraft," *IEEE Transactions on Aerospace and Electronic Systems*, Vol. 57, No. 2, 2021, pp. 1288–1300. https://doi.org/10.1109/TAES.2020.3040518.

[16] Ye, D., and Yang, G.-H., "Adaptive fault-tolerant tracking control against actuator faults with application to flight control," *IEEE Transactions on control systems technology*, Vol. 14, No. 6, 2006, pp. 1088–1096. https://doi.org/10.1109/TCST.2006.883191.

[17] Nabi, H., Lombaerts, T., Zhang, Y., van Kampen, E., Chu, Q., and de Visser, C. C., "Effects of structural failure on the safe flight envelope of aircraft," *Journal of Guidance, Control, and Dynamics*, Vol. 41, No. 6, 2018, pp. 1257–1275. https://doi.org/10.2514/1.G003184.

[18] Bhatia, R., *Matrix Analysis*, Vol. 169, Springer New York, 1997. https://doi.org/10.1007/978-1-4612-0653-8.

[19] Su, W.-C., Drakunov, S., and Ozguner, U., "An O(T/sup 2/) boundary layer in sliding mode for sampled-data systems," *IEEE Transactions on Automatic Control*, Vol. 45, 2000, pp. 482–485. https://doi.org/10.1109/9.847728, URL http://ieeexplore.ieee.org/document/847728/.

[20] Efimov, D., Cieslak, J., Zolghadri, A., and Henry, D., "Actuator fault detection in aircraft systems: Oscillatory failure case study," *Annual Reviews in Control*, Vol. 37, No. 1, 2013, pp. 180–190. https://doi.org/10.1016/j.arcontrol.2013.04.007.

[21] Zhang, Y., De Visser, C., and Chu, Q., "Aircraft damage identification and classification for database-driven online flight-envelope prediction," *Journal of Guidance, Control, and Dynamics*, Vol. 41, No. 2, 2018, pp. 449–460. https://doi.org/10.2514/1.G002866.

[22] Nguyen, L. T., *Simulator study of stall/post-stall characteristics of a fighter airplane with relaxed longitudinal static stability*, Vol. 12854, National Aeronautics and Space Administration, 1979.

[23] Chang, J., Cieslak, J., Guo, Z., and Henry, D., "On the synthesis of a sliding-mode-observer-based adaptive fault-tolerant flight control scheme," *ISA transactions*, Vol. 111, 2021, pp. 8–23. https://doi.org/10.1016/j.isatra.2020.10.061.